JGR Earth Surface

RESEARCH ARTICLE
10.1029/2024JF007688

Effects of Tidal Range and Significant Wave Height on Delta Development

Ewan Sloan[1], **Nicholas Dodd**[1], **and Riccardo Briganti**[1]

[1]Department of Civil Engineering, University of Nottingham, Nottingham, England

Key Points:

- Idealized numerical modeling of river discharge under varied waves and tides suggests limits beyond which delta formation is prevented
- Distinct mechanisms of delta formation under larger waves and tides than those modeled in previous studies are elucidated
- Alongshore diffusion by combined waves and tides is proposed as an explanatory mechanism by which delta formation is inhibited or prevented

Supporting Information:

Supporting Information may be found in the online version of this article.

Correspondence to:

E. Sloan,
ewan.sloan@nottingham.ac.uk

Citation:

Sloan, E., Dodd, N., & Briganti, R. (2024). Effects of tidal range and significant wave height on delta development. *Journal of Geophysical Research: Earth Surface*, *129*, e2024JF007688. https://doi.org/10.1029/2024JF007688

Received 15 FEB 2024
Accepted 15 AUG 2024

Author Contributions:

Conceptualization: Ewan Sloan, Nicholas Dodd, Riccardo Briganti
Data curation: Ewan Sloan
Formal analysis: Ewan Sloan, Nicholas Dodd
Funding acquisition: Nicholas Dodd, Riccardo Briganti
Investigation: Ewan Sloan
Methodology: Ewan Sloan, Nicholas Dodd, Riccardo Briganti
Project administration: Nicholas Dodd
Software: Ewan Sloan
Supervision: Nicholas Dodd, Riccardo Briganti
Validation: Ewan Sloan
Visualization: Ewan Sloan
Writing – original draft: Ewan Sloan

Abstract Only around 40% of rivers globally have deltas, but the conditions which inhibit or facilitate river delta formation are not well understood. Many studies have investigated the response of delta development to marine and river conditions. However, few have investigated the limits of such processes beyond which delta formation may be prevented, and none have done so using numerical modeling. This is in part due to ambiguity in the definition of the term "delta," which can make identification difficult in ambiguous cases. Here we propose a systematic method for identifying deltas, based on: accumulation of sediment above the low tide water level; proximity of such deposits to the initial coastline; and the presence of active channels. We run 42 simulations with identical river (1280 m^3s^{-1}) and sediment (0.048 m^3s^{-1}) discharges, under combinations of significant wave height and tidal range typical for coasts globally, and determine if/when a delta is formed by this definition. Where deltas do form, we classify four formational regimes—river-controlled, river/tide-controlled, wave-controlled, and wave/tide-controlled—and discuss the mechanisms of delta development for each regime. Furthermore, we find that, under the discharge conditions considered, delta formation is prevented for combinations of, approximately, significant wave heights of 2.0 m and tidal ranges ≥3.0 m. We hypothesize that inhibition of delta formation can be explained as a consequence of sufficient marine-driven alongshore sediment transport. This is tested by deriving a 1D alongshore sediment diffusion equation, and comparing predictions made using this formula to the cross-shore integrated sediment volumes of the simulations.

Plain Language Summary River deltas are accumulations of sand and/or silt that form where rivers discharge to the ocean. Not all rivers form deltas, however, and the conditions that allow or prevent delta formation are not well understood. Here, we run a series of computer simulations modeling a river with unchanging discharge of water and sand, discharging into a marine basin featuring varying combinations of waves and tides. We propose an approach to defining precisely when a delta is or is not present, and apply this in order to determine when/if deltas form in our simulations. The results of these simulations are used to identify the limits of wave height and tidal range beyond which delta formation may be prevented under the discharge conditions modeled. These limits are found to exist at, approximately, combinations of wave heights of around 2.0 m and tidal ranges of 3.0 m or more. We also discuss the ways in which the growth of deltas varies under different combinations of waves and tides. Finally, we use a mathematical formula to test the idea that delta formation may be prevented when sediment is driven alongshore away from the river mouth by waves and tides faster than it can accumulate.

1. Introduction and Background

River deltas are fertile, low-lying coastal areas, which have long been settled and exploited by the human population. By one recent estimate, over 300 million people live directly on deltas globally (Edmonds et al., 2020). Despite the importance of deltas, the conditions which inhibit or facilitate their development are not well understood. Many rivers do not produce deltas at all (Caldwell et al., 2019), and most have been subjected to human interference through river management—for example dam building and diversion for irrigation—leading to changes in patterns of sediment transport and river discharge with repercussions for delta formation (Nienhuis et al., 2020; Saito et al., 2007; Syvitski et al., 2005). Taken in combination with climate change induced effects such as sea level rise and changes to weather patterns (Fox-Kemper et al., 2021; Seneviratne et al., 2021), developing our understanding of the processes which control delta development—and the potential of these processes to inhibit or prevent formation—will help us to protect and perhaps restore these vulnerable environments.

Writing – review & editing: Ewan Sloan, Nicholas Dodd, Riccardo Briganti

1.1. Background on Delta Forming Processes

Broadly, there are three dominant sediment transporting processes which affect delta formation: river discharge, waves, and tides (Bird, 2008). Rivers deliver the majority of sediment required for a delta to form, while waves and tides induce changes to patterns of sediment transport and deposition, hence exerting control on the resulting morphology (see e.g. Anthony, 2015; Broaddus et al., 2022; Leonardi et al., 2013; Nienhuis et al., 2018; Orton & Reading, 1993). Based on their observed morphology, deltas have long been qualitatively categorized as wave-, tide-, or river-dominated. Elongated-channel or "birds-foot" type deltas are associated with river-dominance (and sediment cohesiveness), cuspate type deltas with wave-dominance, and open, estuarine type deltas with tidal-dominance (Galloway, 1975; Orton & Reading, 1993). Despite the ubiquity of these classifications in recent literature, they remain broadly qualitative, although some recent studies have taken steps toward formalizing and quantifying them (Nienhuis et al., 2015, 2018, 2020).

Delta formation is commonly characterized as resulting primarily from two distinct formational processes: mouth-bar induced channel bifurcation (splitting), and avulsion (see e.g. Edmonds & Slingerland, 2010). Bifurcation occurs where sediment carried within the discharging jet at the end of a channel is deposited to form a central bar around which flow diverts, leading to channel branching (Edmonds & Slingerland, 2007). Avulsion occurs where an existing channel overtops its banks at some location along its length, leading to the full or partial abandonment of that channel in favor of one or more alternative flow paths (Hoyal & Sheets, 2009). The mechanisms of avulsion are complex but predominantly follow on from downstream channel lengthening and mouth bar growth, which may in some circumstances lead to upstream propagating water level increases and associated bed level increases related to in-channel sediment deposition. Such increases may in turn result in a channel overtopping its banks, leading to the onset of the avulsion process (Edmonds et al., 2009; Hoyal & Sheets, 2009). Mouth-bar formation is affected by both waves and tides. Waves affect mouth bar formation through two mechanisms: first, by deflecting or spreading the discharging jet at a channel mouth; and second, by mobilizing sediments directly in shallow water and hence locally increasing sediment transport rates (Liu et al., 2020; Nardin & Fagherazzi, 2012). In general, these effects lead to a slowing of mouth bar formation as more sediment bypasses the river mouth to be deposited in the basin (Geleynse et al., 2011; Jerolmack & Swenson, 2007). Where this occurs, channels increase in length more slowly and sediment—which is no longer deposited to form a mouth bar—is now distributed more broadly throughout the margins of the delta, leading to smoother shoreline (Ratliff et al., 2018). In some circumstances however, where waves are small and travel opposite to the mean direction of the discharging jet, mouth bar formation has been shown to occur up to 40% faster in comparison to the equivalent situation without waves (Nardin et al., 2013). Increasing tidal variation generally leads to the formation of wider mouth bars which, under very large tidal ranges, may themselves be split in half during ebb tides (Leonardi et al., 2013). Tides are also associated with the development of wider and deeper channels within a delta and an increased stability of channel splits—that is, both downstream arms of a channel split are maintained under tidal forcing rather than one becoming inactive (Hoitink et al., 2017; Iwantoro et al., 2020). How these processes may, if vigorous enough, suppress delta formation is less clear.

1.2. Objectives of This Study

Although many authors have investigated wave and tidal effects on sediment-discharging rivers through numerical modeling, they have typically done so with the intention of investigating how such processes shape deltas; hence they model conditions under which deltas are certain to form. Such studies have modeled delta formation as affected by: waves without tides (Gao et al., 2018, 2019, 2020; Geleynse et al., 2011; Lageweg & Slangen, 2017; Liu et al., 2020); tides without waves (Geleynse et al., 2011; Guo et al., 2015; Lageweg & Slangen, 2017; Rossi et al., 2016; Zhou et al., 2020); or combinations of small waves and tidal ranges (Broaddus et al., 2022). Despite the existence of many rivers that do not form deltas, few authors have sought to identify the limits of these processes beyond which delta formation may be prevented from occurring, and none, to our knowledge, have done so using numerical models. One recent field-study investigated 5,399 rivers globally, and found that only around 40% of these rivers had deltas (Caldwell et al., 2019). Furthermore, many existing deltas are shrinking or stagnating due to anthropogenically induced decreases in sediment flux and the effects of climate change (Nienhuis et al., 2020; Saito et al., 2007; Syvitski et al., 2005). Given the apparent shrinking of many of the world's deltas, as well as the lack of numerical modeling studies on delta formation under higher energy waves and tides, this study aims to address this gap by developing understanding of how these processes control, and potentially slow or prevent delta development.

Here, we use the process-based numerical model Delft3D 4 (Deltares, 2021a, 2021b) in order to investigate how tides and waves affect the development of river deltas within a range of idealized simulations. The primary objective of our work is to determine if there exist limits of significant wave height and/or tidal range above which delta formation is prevented, and to elucidate the relevant processes where (if) this is found to be the case. To this end, we first investigate how delta development is affected under increasing values of wave height and tidal range, both independently and in combination, leading to the identification of four distinct regimes of delta formation. We then discuss the mechanisms by which delta formation is prevented in our simulations with the largest tidal ranges and wave heights, hence identifying a fifth regime of delta-suppression. Comparison is also made to the field-data analysis of Caldwell et al. (2019).

Finally, we note that determining whether or not a delta has formed requires a precise definition of what a delta is. Existing definitions are inconsistent—see for example, Syvitski et al. (2022) for some history and discussion of the term "delta." Here we define our own criteria for delta identification (Section 2.3), but acknowledge that we may in some circumstances classify (or reject) certain morphologies as deltaic, which might be classified differently under alternative definitions.

2. Methodology

Here we describe the model and its setup (Sections 2.1 and 2.2), as well as our approach to defining and analyzing the morphological outputs of our simulations (Sections 2.3 and 2.4).

2.1. Model Description

All simulations are run using the process-based numerical model Delft3D 4. Here we use two distinct modules of Delft3D 4—FLOW and WAVE—run in a coupled configuration so as to allow for the modeling of waves, tides, and sediment transport. Hydrodynamics are calculated in FLOW using the (depth-averaged) shallow water equations, and sediment transport with the Soulsby/Van Rijn equations. Wave states are calculated in a quasi-stationary mode with a spectral action balance equation in WAVE. For details of the equations used, the reader is referred to the Delft3D documentation (Deltares, 2021a, 2021b), and Text S1 in Supporting Information S1.

2.2. Model Setup

We ran 42 numerical simulations, designed to investigate the effects of different combinations of wave height and tidal range on the processes that form deltas on open coasts. In order to simplify analysis and retain a reasonable scope, the parameter space is restricted in a number of ways. River discharge Q_0 [m^3s^{-1}] and sediment discharge Q_{sed} [m^3s^{-1}] are held constant, both within and between simulations. Waves are modeled with a shore-normal mean direction and narrow spread at the offshore boundary, with the only wave-related parameter varied being significant wave height H_s [m]. Tides are modeled with an approximately semidiurnal period ($T_t = 12.5$ hr) and shore-normal direction, such that no net alongshore tidal currents are induced, and with the only tide-related parameter varied being tidal range H_t [m].

Given the wide range of input parameters used in Delft3D, it is not feasible to include an exhaustive account of the preliminary sensitivity testing and calibration informing the setup presented in this Section. In brief, such testing included: transport formulas; wave spreading; FLOW-WAVE coupling period; morphological acceleration factor; WAVE operational mode (stationary or non-stationary); wave frequency spectra; wave directional grid setup; boundary types (e.g., Dirichlet, Neumann, Riemann invariant); cell drying/flooding threshold depth; model spin-up; sub-grid scale turbulence; sediment bed layer setup, dry cell erosion factor; and secondary (helical) flow. Some of these aspects are discussed further within Text S2 in Supporting Information S1.

We use the findings of Caldwell et al. (2019) to inform the parameters used in our numerical models, so as to give a range of both positive and negative predictions of delta occurrence, while also covering combinations of H_s and H_t typical of the environments into which most of the world's rivers discharge. Caldwell et al. (2019) related delta presence for 5,399 rivers to (mean annual) Q_0, Q_{sed}, H_s, and H_t. Larger Q_0 and Q_{sed} were found to increase the likelihood of a delta being present, while larger H_s and H_t were found to decrease likelihood of a delta being present. Based on this analysis, Caldwell et al. (2019) proposed a formula for estimating the probability π_Δ of a given river forming a delta:

$$\pi_\Delta = \frac{\exp(1.45 + 0.000589\langle Q_0\rangle + 2.56\langle Q_{sed}\rangle - 0.975\langle H_s\rangle - 0.187\langle H_t\rangle)}{1 + \exp(1.45 + 0.000589\langle Q_0\rangle + 2.56\langle Q_{sed}\rangle - 0.975\langle H_s\rangle - 0.187\langle H_t\rangle)} \quad (1)$$

where $\langle Q_0\rangle$ is mean annual volumetric river water flux [m^3s^{-1}]; $\langle Q_{sed}\rangle$ is mean annual volumetric river sediment flux [m^3s^{-1}]; $\langle H_s\rangle$ is the annual mean of hourly significant wave heights [m]; and $\langle H_t\rangle$ is mean annual tidal range [m]. Values of π_Δ range from 0 to 1, with values greater than 0.5 considered to represent conditions for which a delta is likely to form and values less than 0.5 to represent those for which a delta is unlikely to form. We model combinations of H_s up to 2 m, and H_t up to 6 m, giving the range of π_Δ values shown in Figure 2, and broadly representing marine conditions typical for such environments globally (Figure 1). For the purposes of this study, it is assumed that steady H_s values produce equivalent morphologies to respective unsteady H_s values with identical temporal means, and that fixed-amplitude tides produce equivalent morphologies to real tides in which the lunar semidiurnal (M2) component is dominant.

Various simulation parameters are summarized in Table 1. We first note that volumetric discharges vary enormously between real rivers. As the world's highest-discharging rivers almost universally produce deltas (Caldwell et al., 2019), Q_0 is set to a modest rate of 1280 m^3s^{-1}, for which delta presence is less certain (a value which also leads to a range of π_Δ values greater than or less than 0.5, as well three simulations giving π_Δ values of approximately 0.5; useful in testing how well Equation 1 agrees with our simulations). This discharge rate is representative of rivers such as the Chao Phraya, Copper, Ebro, Po, and Vistula (Syvitski & Saito, 2007), and the width of the modeled river is typical of rivers with this discharge (Frasson et al., 2019). The depth-averaged fine sand mass concentration $\bar{c}_{mass} = 0.1$ [kgm^{-3}] (volumetric concentration $\bar{c} = 3.77 \times 10^{-5}$ m^3m^{-3}) at the inflow is at the lower end of concentrations seen in such rivers (Milliman & Farnsworth, 2011; Syvitski & Saito, 2007) (see Figure 3). This value is selected in order to ensure that some simulations are predicted not to form deltas according to Equation 1. Additionally, both Q_0 and $\bar{c}$ are also chosen for comparability to prior numerical studies of deltas, for which discharges and concentrations are often close to these values (e.g., Burpee et al., 2015; Caldwell & Edmonds, 2014; Edmonds & Slingerland, 2010; Gao et al., 2019; Geleynse et al., 2010, 2011; van der Vegt et al., 2016). We assume here that the application of these temporally unvarying discharge boundaries produces results that do not differ substantially from equivalent temporally varying conditions with identical means. The fine sand median diameter $D_{50,f} = 0.125$ mm is in the typical range for many rivers, particularly those with discharges close to our selected value of Q_0 (Orton & Reading, 1993; Syvitski & Saito, 2007), and is also comparable to values used in previous numerical modeling studies on deltas (e.g., Broaddus et al., 2022; Edmonds & Slingerland, 2010; Gao et al., 2019; Geleynse et al., 2010; van der Vegt et al., 2016).

Nearshore sediment distributions are generally characterized by onshore coarsening of sediments. Rather than attempt to precisely model this gradation throughout the model domain, we instead choose a single coarse sand of $D_{50,c} = 1.0$ mm (distinct from the fine sediment fraction $D_{50,f}$ modeled as a river input) and set the sediment diameter to this value in all initially erodible regions of sediment in the domain (see Section 2.2.2). The use of this coarse sediment fraction in the basin allows for some incision of the expected delta channels below the initial bed level, while also minimizing reworking of initial bed sediments—a result of the higher mobilization stresses required for the coarser sediment compared to the fine. Setting the simulations up in this way simplifies the analysis of the morphologies produced, particularly under the higher energy marine conditions modeled. Note that we do not model sediments in the cohesive range ($D_{50} < 0.064$ mm). The presence of cohesive sediments may be expected to have two significant effects on delta-forming processes: a wider spread of sediments beyond discharging river mouths, as cohesive sediments in general have a slower settling velocity than non-cohesive; and an increase in the critical bed shear stresses required for remobilization (in Delft3D, based on a constant value specified by the user; in reality, somewhat dependent upon the degree of consolidation over time). These effects lead to slower mouth bar growth, as well as reduced likelihood of avulsions (Burpee et al., 2015; Caldwell & Edmonds, 2014; Edmonds & Slingerland, 2010; Orton & Reading, 1993). As the proportion of cohesive sediments increases, morphologies would therefore be expected to tend toward the development of fewer, longer channels (Geleynse et al., 2011; Guo et al., 2015). As such, given that the presence of cohesive sediments would be expected to produce different morphological outcomes in comparison to simulations in which they are absent, the results presented herein should only be considered valid for rivers in which the cohesive fraction is negligible with respect to the non-cohesive.

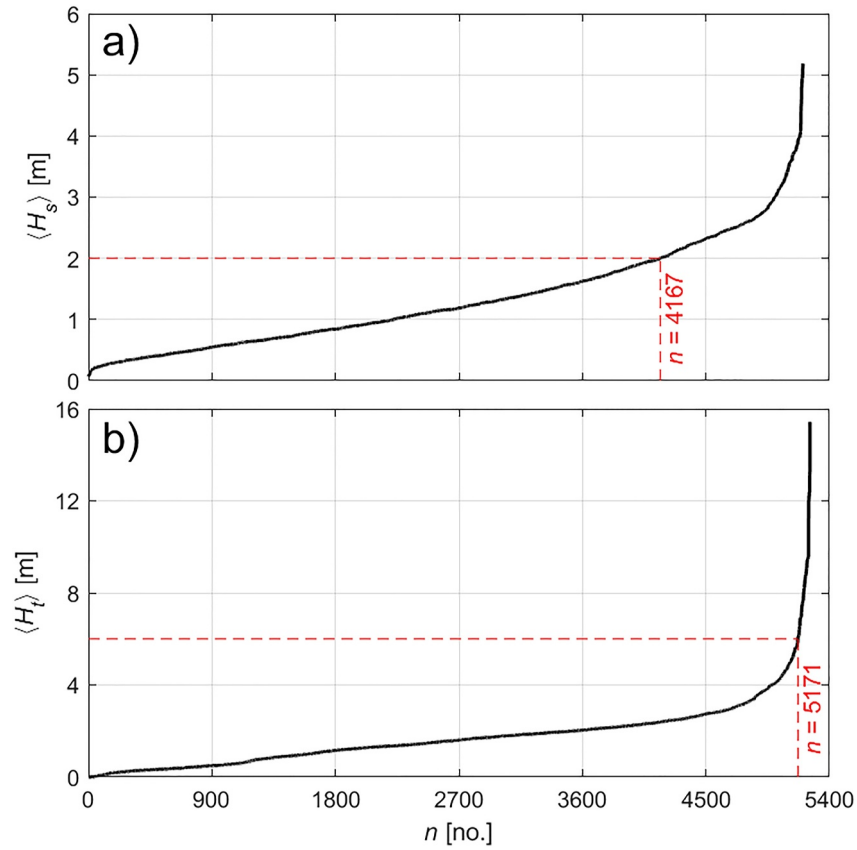

Figure 1. Values of: (a) $\langle H_s \rangle$; and (b) $\langle H_t \rangle$ associated with rivers investigated by Caldwell et al. (2019). Data are arranged in ascending order of magnitude. Red dashed lines indicate the maximum values of $\langle H_s \rangle$ and $\langle H_t \rangle$ used in the present study, as well as the approximate proportion of the data set covered by the ranges modeled. (Note that there are gaps in the data set, hence there are fewer than 5,399 values in each subplot).

We emphasize that the decision not to include cohesive sediments alongside non-cohesive is in many ways a practical consideration, as their presence introduces complexity in terms of sediment interaction, such as the hiding/exposure of finer sediments by coarser ones. As argued earlier, we use an idealized modeling approach as we believe this allows for the easier interpretation of the effects of variation in H_s and H_t, which is the principle focus of this study. This extends to the simplified representation of sediment diameter and distribution.

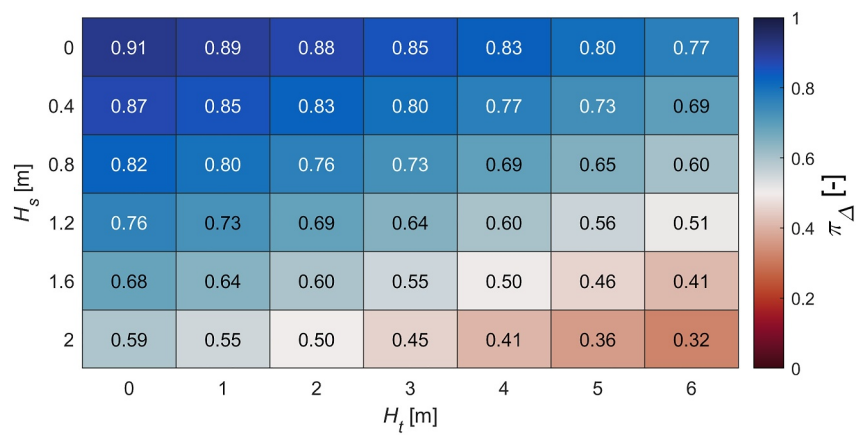

Figure 2. Values of π_Δ calculated using Equation 1 for all simulations.

Table 1
Model Parameters

	Symbol	Value	Unit
Physical Parameters			
Upstream discharge	Q_0	1,280	m^3s^{-1}
Water density	ρ_0	1,000	kgm^{-3}
Depth-averaged concentration at inflow	$\bar{c}_{mass}$	0.1	kgm^{-3}
Sediment flux at inflow	Q_{sed}	0.048	m^3s^{-1}
Grain particle density	ρ_s	2,650	kgm^{-3}
Tidal period	T_t	12.5	hr
Sand dry bulk density	ρ_{bulk}	1,600	kgm^{-3}
Fine sand median diameter	$D_{50,f}$	0.125	mm
Coarse sand median diameter	$D_{50,c}$	1.0	mm
Numerical Parameters			
Time-step	Δt	9	s
Morphological acceleration factor	f_m	175	-
Chézy roughness coefficient	C	45	$m^{1/2}s^{-1}$
FLOW-WAVE coupling period	-	60	min

Furthermore, we note that comprehensive global data on the size and distribution of sediments transported at river mouths is lacking at present. In general, this makes any argument concerning the precise distribution of sediment adopted difficult to justify, except for specific case studies in which comprehensive data is in fact available.

As salinity variation and related effects such as gravity currents are not accounted for in the 2D depth-averaged model, we use a constant water density $\rho_0 = 1000\ kgm^{-3}$ throughout. Sands are deposited at a dry bulk density $\rho_{bulk} = 1600\ kgm^{-3}$ ($\rho_{bulk} = \rho_s(1-n)$ where $n \approx 0.4$ is porosity of deposited sediments), typical for predominantly sandy mixtures (van Rijn, 1993). This value is also commonly used in prior delta modeling studies (e.g., Baar et al., 2019; Burpee et al., 2015; Edmonds & Slingerland, 2010; Geleynse et al., 2010, 2011). The time-step $\Delta t = 9$ s is selected to satisfy all Courant stability requirements for the model. The morphological acceleration factor f_m is a factor by which all calculated changes to bed sediment mass as a result of entrainment/deposition or bed transport are multiplied, and is used to accelerate morphological development with respect to hydrodynamics. The choice of $f_m = 175$ follows sensitivity testing which revealed that while values of $f_m \leq 175$ did not significantly alter morphological development, higher values led to large sediment mass-balance errors. We use a Chézy roughness coefficient $C = 45\ m^{1/2}s^{-1}$ (equivalent to dimensionless friction coefficient $C_d = g/C^2 = 4.8\dot{4} \times 10^{-3}$) for comparability to prior studies, where this is again a frequently used value (e.g., Burpee et al., 2015; Caldwell & Edmonds, 2014; Edmonds & Slingerland, 2010; Gao et al., 2019; Lageweg & Slangen, 2017). Additional aspects of model setup—those which are not considered essential to understanding of the discussion presented hereafter—are outlined in Text S2 of Supporting Information S1.

All simulations are run for an initial 36 years of morphodynamic development. Simulations that do not form a delta within this time are extended to run for an additional 36 years. In some simulations, a delta does not form within 72 years. While formation of a delta within 72 years in our simulations provides a reasonable basis for supposing that delta formation would also occur in a similar real-world system, non-formation of a delta does not so simply support the conclusion that a delta would never form in a similar real-world system. This is especially true when considering the up-to-millennial timescales over which many real world river deltas have in fact formed. However, as we shall argue in Section 2.3.1, under larger H_s and H_t, sediment may be diffused away from the river mouth at a similar rate to that at which it arrives. This approximate equilibrium supports the notion that delta formation may continue to be prevented in such cases. Based on this observation, we assume that delta-formation has been entirely prevented under the given conditions in non-delta-forming simulations (although we acknowledge that the equilibrium described is somewhat dependent on the constant-boundary approach taken here, and may differ under time-varying conditions). Furthermore, while this assumption may or may not extend to the up-to-millennial timescales of many real deltas, we argue that prevention of delta-formation within multi-decadal timescales—in comparison to the relatively rapid formation seen in lower marine-energy simulations—is in itself a strong enough effect to be classifiable as "prevention." This designation is meaningful insofar as it is of use in guiding human response to the future development of coastal systems into which rivers discharge.

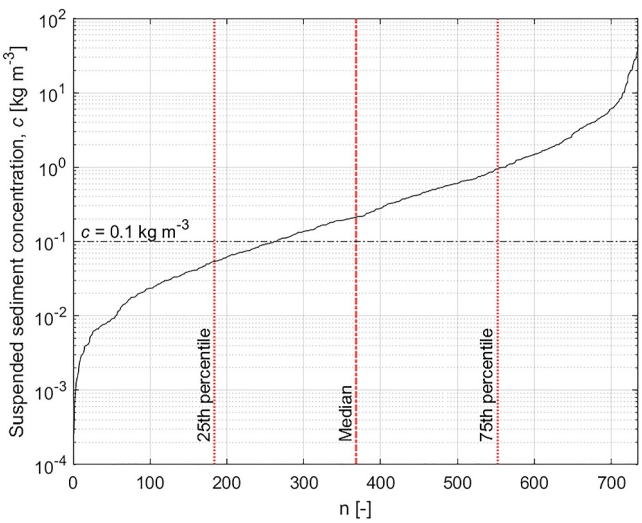

Figure 3. Suspended sediment concentrations (SSCs) for 735 global rivers from Milliman and Farnsworth (2011). Data are arranged in ascending order of SSC. The black dashed line highlights that the modeled concentration from our simulations ($c = 0.1\ kgs^{-1}$) is below the median concentration for rivers globally.

2.2.1. Domain and Grids

The model domain is shown in Figure 4. The FLOW domain comprises: a 19.75 km alongshore × 9.00 km cross-shore basin with a regular grid size of

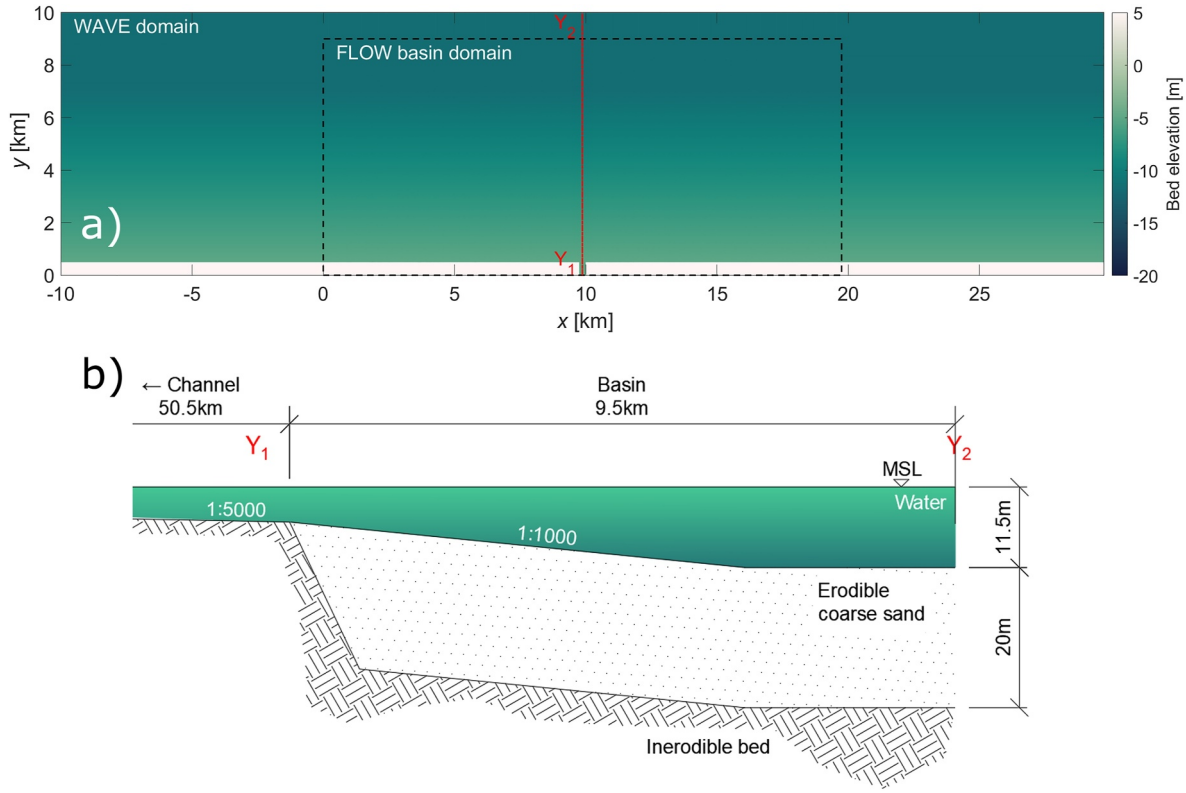

Figure 4. Initial basin bathymetry and domains used in all simulations. Full channel not shown. (a) Plan-view of initial basin, with FLOW basin domain enclosed by black dashed line. Red dashed line indicates location of transect Y_1–Y_2. (b) Transect Y_1–Y_2, showing sketch of channel and basin slope and erodible coarse sand layer. Water level shown at mean sea level (MSL). Note that the vertical axis is exaggerated by a factor of 100.

25 m × 25 m; and a (1D) feeder channel of 50.00 km length × 0.25 km width, with regular grid size of 250 m × 250 m. The FLOW basin domain is nested in a larger WAVE domain with alongshore dimension 39.75 km × cross-shore dimension 10.00 km, and with regular grid size of 50 m × 50 m. The wide margins in the WAVE domain are included to prevent shadow regions at the lateral WAVE boundaries from affecting the FLOW domain.

This setup allows sufficient space for the deposited sediment mass to develop in most simulations without reaching the outer boundaries. The 25 m × 25 m FLOW resolution is deemed fine enough to minimize the issue of channel grid-alignment which often occurs with rectilinear grids (Baar et al., 2019), including in our own tests of larger grid sizes (see Text S3 in Supporting Information S1). In preliminary simulations, smaller grid sizes showed no appreciable differences in overall observed morphodynamic development, but lead to greatly increased simulation run times.

WAVE requires specification of spectral grids in both the directional and frequency spaces. Here we define 24 logarithmically spaced bins in frequency space ranging from 0.05 to 1.00 Hz, and 18 directional bins oriented at 5° intervals between ±45° from shore-normal. This setup is sufficient to capture the predominantly shore-normal directed wave energy flux (see boundary setup— Section 2.2.3), but does incur small artificial losses of wave energy where refraction would lead to wave energy flux being transferred from the outermost directional bins toward angles >45° from shore-normal (which may happen as the bed evolves). However, sensitivity tests showed negligible differences in morphodynamic development between simulations with a directional grid as described above, and a full 360° grid with 72 directional bins of 5°.

2.2.2. Initial Bathymetry

All simulations start from the same initial bathymetry (see Figure 4). The basin has bed level −5 m at Y_1 nearshore (relative to mean sea level) decreasing to −11.5 m at Y_2 offshore with a transitional slope of 1:1000.

This −11.5 m bed level is maintained in the most offshore 3 km strip of the basin (y = 7000 m to 10000 m). Additionally, random perturbations with a uniform distribution from 0 m to −0.05 m are applied throughout the basin. The basin itself is also partially erodible; a layer of up to 20 m thickness of coarse sand ($D_{50,c}$ = 1 mm) is available throughout, starting from 0 m layer thickness adjacent to the initial coastline and increasing linearly to a layer thickness of 20 m over a distance of 1 km (y = 500 m to y = 1500 m, see Figure 4b). The 20 m layer thickness is maintained offshore from this point. A 500 m wide, 20 m high strip of the same coarse sand is added along the bottom edge of the basin, delineating the initial coastline.

This schematized bathymetry is considered to represent the inner region of a shelf sea into which rivers commonly discharge. The 1:1000 slope of the initial basin is of relatively low steepness for nearshore slopes globally (Athanasiou et al., 2019), but is steeper than often seen in comparable numerical modeling studies of deltas, where slopes often range between 1:2,000 and 1:5,000 (e.g., Burpee et al., 2015; Edmonds & Slingerland, 2010; Guo et al., 2015; Zhou et al., 2020). The choice of a relatively gentle 1:1000 slope (with respect to real nearshore slopes) is partially a compromise to allow for faster morphological development, as this reduces the accommodation space within the basin. This allows for sediment to spread over a larger area in a reduced length of time, reducing the computational expense of the simulations.

The feeder channel exists primarily to deliver water and sediment to the basin. The channel has slope 1:5000 and a total initial length of 50.5 km. This length is imposed in order to allow for tidal inundation and related discharge attenuation of the river in tidal simulations (Were tides able to propagate to the discharging boundary, the constant discharge boundary condition would become unrealistic). The bed of the channel is inerodible so as to ensure precise control of—and parity between—mean sediment fluxes from the channel into the basin between simulations. The slope and 1D configuration of the channel are chosen so as to prevent sediment deposition within the channel, also helping to ensure parity of sediment fluxes. Additionally, this approach prevents second-order effects of tidally influenced river-braiding or similar phenomena from affecting depositional morphologies within the basin, allowing for observed morphological differences to be related purely to first-order wave and tidal effects on basin morphodynamics.

2.2.3. Boundary Conditions

We wish to emphasize that, while we have generally adopted a constant boundary approach throughout (tides are somewhat of an exception as these are harmonic and hence quasi-constant), the differences between constant boundaries and equivalent temporally varying ones are potentially large (see e.g., Guo et al., 2015; Gao et al., 2018, 2019, for some discussion of temporal variation of boundaries). While temporally varying boundary conditions may produce morphologies that more closely resemble those of real coasts and deltas, such a setup introduces a significant level of complexity around the interpretation of process interaction, depending on, for example, whether peaks occur concurrently or in alternating patterns. This would make the interpretation of the developmental effects of each process more difficult to discern. As such, the use of a constant boundaries is argued here to be appropriate, as it allows for easier inference of the ways in which individual processes affect morphological development.

2.2.3.1. FLOW—Hydrodynamic Boundaries

River discharge $Q_0 = 1280\ \mathrm{m^3 s^{-1}}$ is imposed at the head of the river, using a temporally unvarying Dirichlet discharge boundary. At the lateral edges of the basin, Neumann boundaries are applied with respect to free surface elevation ζ [m], set to give boundary-normal gradients of $\partial\zeta/\partial x = 0$. Offshore, a harmonically varying Riemann invariant boundary is applied with period T_t = 12.5 hr and with a maximum value chosen to give the desired tidal range. The Riemann invariant R^+_{D3D} [$\mathrm{ms^{-1}}$] boundary in harmonic form is: $R^+_{D3D}(t) = -\sin(2\pi t/T_t)\left(\bar{u} + \zeta\sqrt{g/\bar{h}}\right)$ where t is time [s]; $\bar{u}$ is depth-averaged velocity [$\mathrm{ms^{-1}}$]; and $\bar{h}$ is mean water depth [m]. From linear wave theory, it can be shown that $\bar{u} = \zeta\sqrt{g/\bar{h}}$ in shallow water, hence the harmonic Riemann boundary equation may be re-written as $R^+_{D3D}(t) = -\sin(2\pi t/T_t)\,2\zeta\sqrt{g/\bar{h}}$. This boundary setup represents a coast-normal propagating tidal wave which is fully reflected at the coastline. As such, ζ is set equal to $H_t/4$ in order to give the desired tidal range H_t.

An alongshore propagating tidal wave may be expected to produce slightly different outcomes to the cross-shore propagating one, particularly due to the net-alongshore currents which may be induced by the former. However,

Geleynse et al. (2011) noted that the differences between cross-shore and alongshore propagating tides (with $H_t = 3$ m) with respect to delta development were remarkably small in their simulations.

2.2.3.2. FLOW—Sediment Transport Boundaries

Fluvial sediments enter the model domain at the head of the feeder channel. This is achieved by setting a fine sediment ($D_{50,f} = 0.125$ mm, $\rho_s = 2650$ kgm^{-3}) mass concentration $\bar{c}_{mass} = 0.1$ kgm^{-3}. Suspended sediment concentration at all remaining boundaries is set to $\bar{c}_{mass} = 0.0$ kgm^{-3}. The model setup is such that bedload fluxes into the domain are nil or negligible at all boundaries.

2.2.3.3. WAVE—Wave Spectrum Boundaries

Where waves are modeled, these are generated at the offshore boundary of the WAVE-grid using a JONSWAP spectrum with peak enhancement factor $\gamma_0 = 3.3$, peak period $T_p = 5$ s, shore-normal mean direction of propagation, and $\cos^{16}$ directional spread (Deltares, 2021b; Roelvink & Reniers, 2011). Selection of $T_p = 5$ s is partially for comparability to previous studies, where this value has commonly been used (e.g., Broaddus et al., 2022; Gao et al., 2019; Geleynse et al., 2011; Lageweg & Slangen, 2017; Liu et al., 2020), and partially based on wave data from Mangor et al. (2017). Selection of $\cos^{16}$ wave spreading followed sensitivity testing of a range of exponents, which revealed that narrower spreads ($\cos^{16}$, $\cos^{50}$ and $\cos^{500}$ were tested) lead to spurious wave-fields within the FLOW-domain, characterized by alternating peaks and troughs of local H_s above or below the boundary value. All other boundaries in the WAVE-domain are closed (i.e., wave spectral density is zero).

2.3. Criteria for Identifying Deltas

One possible reason for the lack of investigation of the limits of delta development is the absence of a consistent, precise, and uniformly adopted definition of what a river delta actually is, which can make their identification difficult in ambiguous cases (Syvitski et al., 2022). A common simple definition is that a delta is any mass of sediment deposited where a river discharges that is both contiguous and partially emergent at low tide (Caldwell et al., 2019; Galloway, 1975; Syvitski et al., 2022; Wright, 1985). This definition is appealing for its simplicity, but is here considered too imprecise to make a realistic determination of which morphologies are or are not deltas in ambiguous cases. As such, we define two additional, systematic criteria for identifying deltas with respect to regions of emergent sediment: first, that such regions should lie inland of the shoreline rather than form isolated bars or islands offshore (a distinction that requires a methodology for identifying said shoreline and hence distinguishing between such areas—see below); and second, that such regions should be incised by active channels (where "active" means that water in a given channel has a non-zero residual, i.e. tidally averaged, current), extending from the initial river.

In order to classify morphologies as deltas following the above criteria, the locations of low tide lines must first be identified. To this end, the opening angle method (OAM) is used (Shaw et al., 2008). We apply the OAM with a depth threshold of 0.11 m to delineate wet versus dry cells, and cut-off angle of 70° to define the location(s) of low tides lines (see Shaw et al., 2008). The 0.11 m threshold was selected primarily for reasons related to limitations of the model. Specifically, Delft3D uses a threshold depth of 0.1 m, below which any bedload transport into or out of a given cell is prevented, as well as any deposition (entrainment) of sediment from (into) the water column. This essentially fixes the bathymetry where local water depth reduces below 0.1 m, even if the cell is still hydrodynamically active. As such, we apply this value +10% when applying the OAM so as to avoid erroneously counting morphologically inactive (functionally dry) cells as wet. This is a particular risk in non-tidal simulations, wherein expansive regions exist with depths close to this value. Sensitivity testing of this threshold was performed, but the simulations were not generally sensitive to increases in this value. Non-tidal simulations with small or no waves did show sensitivity to reductions in the depth threshold employed for the OAM, but this is to be expected for the reasons described above. The 70° cut-off angle follows the recommendation of Shaw et al. (2008).

Applying the OAM at low tide will produce one contour encompassing the initial coast and adjoining emergent deposits—this contour is the low tide shoreline—as well as a number of closed contours encompassing offshore emergent bars or islands. The shoreline denotes the boundary between onshore and offshore areas. These concepts are illustrated in the simple schematic shown in Figure 5. Note that the terms "shoreline" and "coastline" are not used as synonyms; we use coastline to refer to the boundary between "solid" land and shore (assumed in our

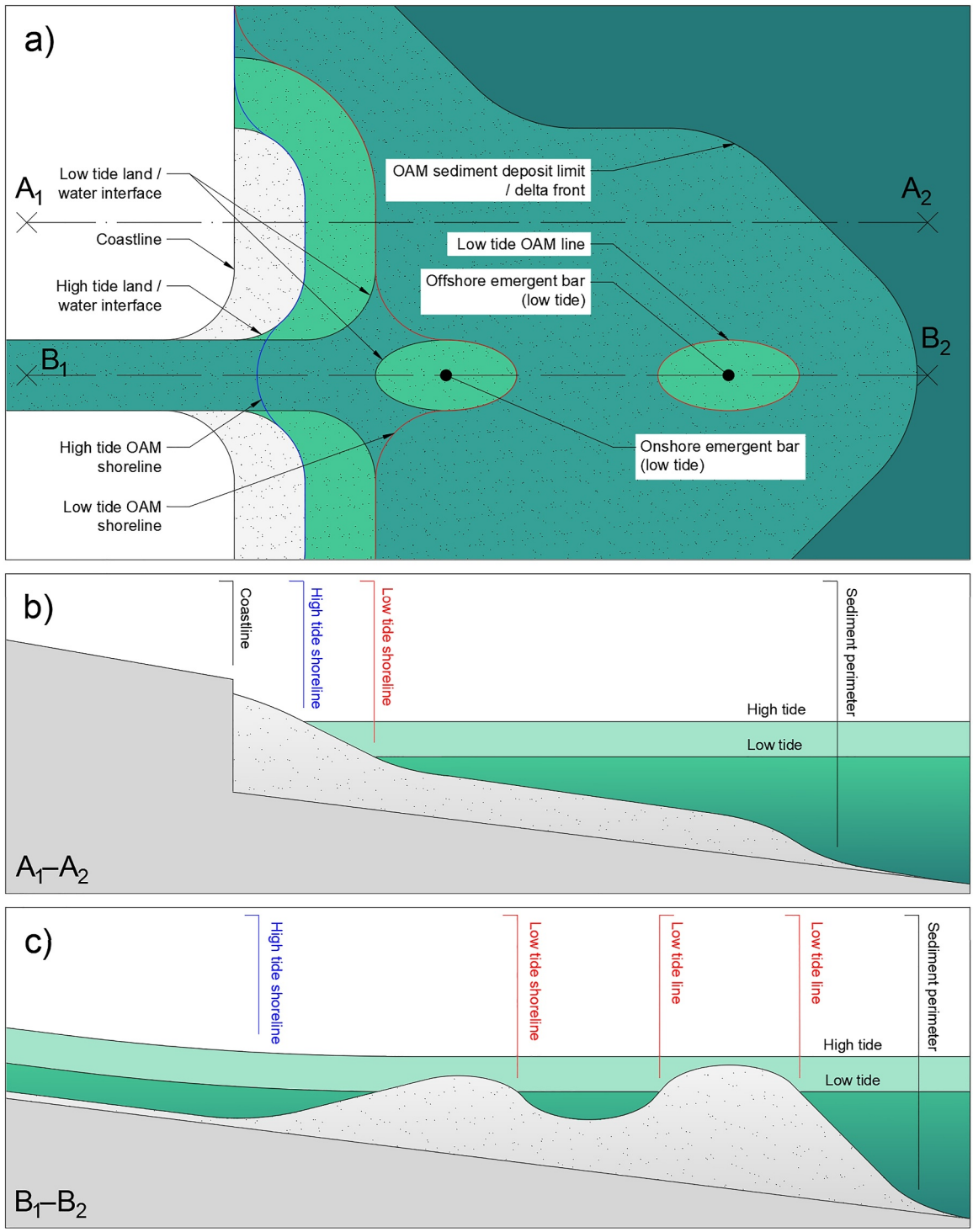

Figure 5. Schematic showing example of the coastline, as well as the low and high tide (shore) lines and sediment mass perimeter, as determined using the OAM. Subfigures show: (a) plan view showing example onshore and offshore bars within a sediment deposit, as distinguished by the locations of the low tide shoreline; (b) transect A_1–A_2; and (c) transect B_1–B_2.

simulations to be located at the boundary between the basin and erodible margin along $y = 0.5$ km), and shoreline to refer to the instantaneous boundary between shore and open water, which varies with tidal water level (see Figure 5 and Bird, 2008).

Actively channelized cells within the low tide area are identified as those exceeding both a characteristic depth and velocity threshold. Here we adopt a mid-tide depth threshold $h_c = (H_t/2) + 0.5$ m, and residual velocity threshold $\bar{u}_c = 0.2$ ms^{-1}. The selected value of h_c is guided by the logic employed by van der Vegt et al. (2016), in that the minimum depth of 0.5 m (at low tide) would give a minimum width-to-depth ratio of 50 for our basin grid-size $\Delta x = \Delta y = 25$ m. This seems a reasonable cut-off for distinguishing channel flow from sheet/overland flow. The selected value of $\bar{u}_c$ is chosen to allow for a degree of tidal asymmetry within a given (inactive) channel or network of channels, as well as expected slight differences in flow-routing between ebb and flood within those same channels. Both of these effects may result in small residual velocities occurring in channels through which river discharge is not being routed. We consider an active channel network to be present when the total area of such cells exceeds 0.2 km^2.

Based on these considerations, we therefore identify a delta as having formed when:

1. A contiguous mass of sediment is deposited near the river mouth;
2. Part of this deposited sediment mass emerges above water at low tide (above local water level for non-tidal cases);
3. At least one area defined by applying the OAM to the emergent deposit(s) adjoins the initial coastline; and
4. Active channels, extending from the initial river, are incised into the region defined by Equation 3.

Where all of the above are true, we classify the entire mass of deposited sediment to be a delta, and the region circumscribed by the low tide shoreline and initial coastline as the delta plain.

2.3.1. Use of the OAM to Determine High Tide Lines and the Extent of the Sediment Mass

The OAM is also used to define the location of high tide lines. As with identification of the low tide shoreline, the single high tide line encompassing the region extending from the initial coastline is identified as the high tide shoreline.

For consistency, the perimeter of the deposited sediment mass is also identified using the OAM. Here, we define the perimeter as the toe of the relatively steep front of deposited sediment (the "delta front" in deltaic morphologies), as this line typically encompasses >99% of the river-delivered sediments. This definition excludes the fine layer of river-delivered sediments which may be deposited far beyond this point in, particularly, the higher wave-energy simulations (the "pro-delta" in deltaic morphologies). In order to omit this thin region, we apply the OAM by first defining a threshold bed level change $\Delta z_c = 0.25$ m with respect to the initial bed level, below which a given cell is considered not to be a part of the deposited sediment mass. We then determine net bed level change Δz [m] per cell with respect to the initial bed level. The OAM is applied to all cells for which $\Delta z \leq \Delta z_c$, with opening angles defined as the sum of all angles traceable through arcs that do not intersect cells for which $\Delta z > \Delta z_c$. The same threshold opening angle $\phi_c = 70°$ is used, with the contour thus defined denoting the outer extent of the sediment mass. For instances in which a given morphology is identified as a delta, this contour also indicates the location of the delta front. The high tide shoreline and sediment mass perimeter are also illustrated in Figure 5.

2.4. Morphodynamic Metrics

We define and track various metrics in order to quantify aspects of morphodynamic development in our simulations. These relate to: overall morphodynamic activity; the number of channel splits occurring; mobility of channels within deltas; and the distribution of deposited sediments. For comparability of results, we analyze all metrics over intervals of tidal period T_t regardless of whether tides are modeled in a given simulation. See also Figure S5 in Supporting Information S1 for schematics illustrating the metrics presented here.

As a measure of overall morphodynamic activity in a simulation, we define non-dimensionalized excess mobility number χ [−], which quantifies the degree of sediment remobilization per tide throughout the domain. This is defined as:

$$\chi(t) = \frac{\sum_{i=1}^{M}\sum_{j=1}^{N}|\Delta z_{i,j}^{-}(t)|}{f_z}$$

Table 2
Time of Delta Formation for All Simulations [yr]

		H_t [m]						
		0.0	1.0	2.0	3.0	4.0	5.0	6.0
H_s [m]	0.0	2.75	1.75	2.00	2.00	1.50	1.50	2.00
	0.4	3.25	3.50	2.25	2.25	2.00	1.50	2.00
	0.8	5.50	6.50	7.50	6.50	11.00	11.50	3.50
	1.2	8.00	9.00	23.50	18.00	19.00	21.50	23.50
	1.6	24.50	33.75	20.00	39.75	62.75	54.75	n/a
	2.0	67.25	51.25	n/a	n/a	n/a	n/a	n/a

Note. In some cases, morphologies fluctuate between meeting and not meeting the criteria for classification as a delta. In these cases, delta formation time is defined as that at which the criteria are satisfied without subsequently returning to a non-deltaic configuration. All times are given to nearest 0.25 years.

where $\sum_{i=1}^{M}\sum_{j=1}^{N}|\Delta z_{i,j}^{-}(t)|$ is the sum of magnitudes of all negative bed level changes per tide at time t [m]; M, N are the number of cells in the x and y directions respectively of the FLOW basin grid; and $f_z = Q_{sed}T_t f_m/\rho_{bulk}\Delta x\Delta y$ [m] is a normalization factor representing the expected net bed level increase per tide, assuming 100% deposition in the basin and no remobilization of sediment. Where $\chi = 0$, this implies that no sediment has been remobilized within the domain. A χ-value of one implies that a volume of sediment has been mobilized within the domain which is equal to the volume of sediment entering the domain in the period of time considered, that is, 12.5 hr (one tidal period). Values greater than one imply a concurrently greater degree of remobilization of sediment within the domain.

We similarly calculate χ_{inner}, defined as the excess mobility number within the low tide shoreline only, in order to further distinguish whether morphodynamic change is occurring within or outside of the low tide area.

We characterize the channel network via two metrics: number of channel splits c_{split} [-], and channel mobility c_{mob} [-]. Channel splits are counted by first determining the active channel network according to the methodology described in Section 2.3. This channel network is then skeletonized (Tejedor et al., 2016), from which the number of branch-points (intersections of three or more channels) in the active network is counted. As we wish to count channel splits (i.e., bifurcations and avulsions) and not confluences (i.e., instances in which one or more channels recombine into a single channel), we subtract the number of regions wholly enclosed by surrounding channels from this count, under the logic that any such enclosed regions arise only as a result of a channel confluence.

Channel mobility is determined from the fractional overlap of the active channel network over successive tides (van der Vegt et al., 2016). It is defined as the total area of currently active channel cells which were not active at the previous time interval, divided by the total area of currently active channel cells. Thus, $c_{mob} = 0$ indicates that the active channel network has not changed over successive tides, and $c_{mob} = 1$ indicates that the active channel network occupies an entirely different region than one tide previously.

Finally, as measures of the distribution of deposited sediments, we determine z-axis centroid elevations and alongshore standard deviations σ_x [km] of net volumetric change in the bed with respect to initial bathymetry.

3. Results

Table 2 shows times of delta formation following the methodology outlined in Section 2.3, and Figure 6 shows the morphology of most of our simulations after ~35.75 yr of development. In six of the 42 simulations, deltas did not form within 72 years; an outcome which aligns well with the predictions made using Equation 1 (Figure 2). Of the six simulations for which deltas were predicted unlikely to occur ($\pi_\Delta < 0.5$), one formed a delta (W1.6T5.0), four did not (W2.0T3.0, W2.0T4.0, W2.0T5.0, and W2.0T6.0), and one experienced a cycle between deltaic and non-deltaic morphology (W1.6T6.0; considered non-deltaic after 72 years). Of the three simulations for which $\pi_\Delta \approx 0.5$, two produced deltas and one did not. Of the remaining 33 simulations, for which $\pi_\Delta > 0.5$, all produced deltas. Generally, larger waves delayed delta formation more than did larger tides. Note that animations showing bathymetry over time for all simulations—including those omitted from Figure 6—can be found in the Supporting Information S1 accompanying this paper.

Without the influence of waves or tidal variation, delta development is controlled only by interaction between river discharge and the growing mass of deposited sediment. Excess mobility $\langle\chi\rangle$ is higher for simulation W0.0T0.0 ($H_s = 0$ m, $H_t = 0$ m) than all tide-only simulations, but lower than most simulations with waves (Figure 7a). $\langle\chi_{inner}\rangle$, $\langle c_{split}\rangle$ and $\langle c_{mob}\rangle$ are all amongst the highest measured for simulation W0.0T0.0 in comparison to all other simulations (Figures 7b, 7c, and 7d). W0.0T0.0 also gives some of the highest values for $\langle c_{split}\rangle$ and $\langle c_{mob}\rangle$. This comparatively high degree of (internal) morphological reworking and channel network splits/mobility suggests a high frequency of bifurcations and avulsions, an apparent result of the absence of external forcing from marine sources. The mechanisms explaining this (and other delta formation processes) are discussed in Section 4.1.

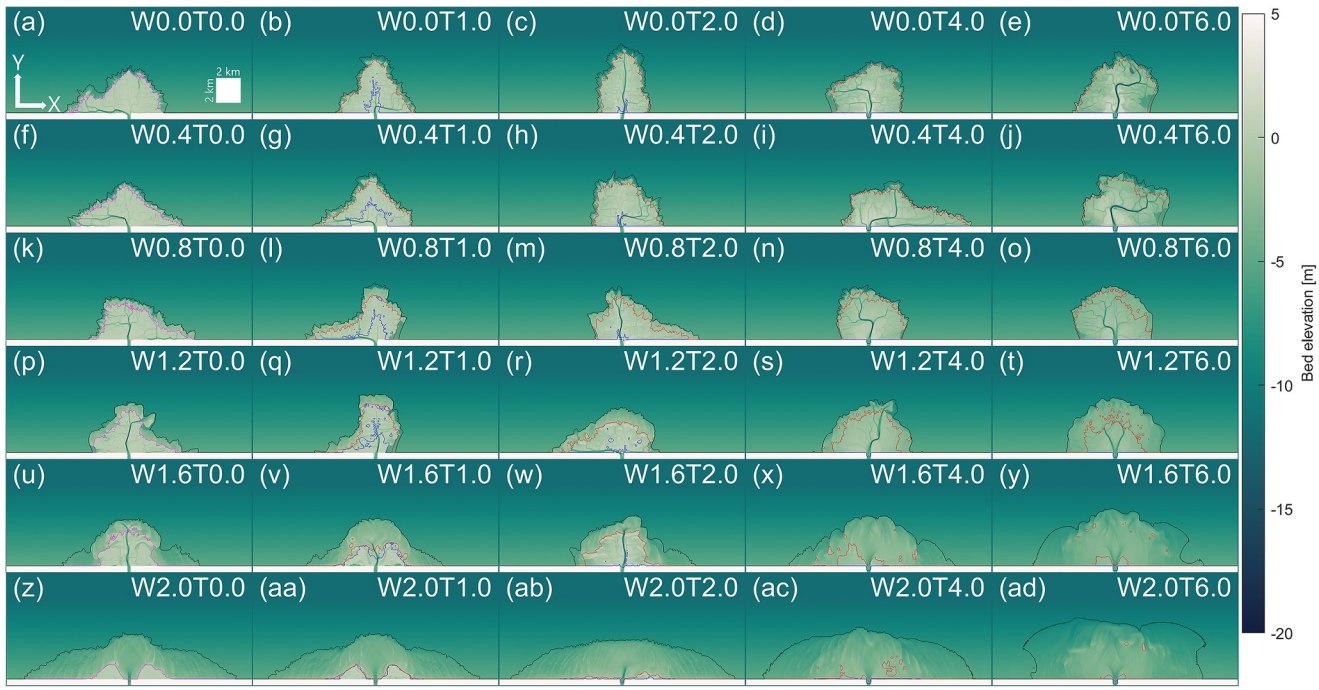

Figure 6. Selected bathymetries at $t \approx 35.75$ yr. Left to right: $H_t = 0.0$ m, 1.0 m, 2.0 m, 4.0 m, and 6.0 m. Top to bottom: $H_s = 0.0$ m, 0.4 m, 0.8 m, 1.2 m, 1.6 m, and 2.0 m. Black lines denote outer extent of sediment mass. Blue lines denote high tide shoreline or bar/island edges. Red lines denote low tide shoreline or bar/island edges. Magenta lines denote generic shoreline or bar/island edges in non-tidal simulations. Simulation IDs are shown on each subplot.

In our wave-only simulations, the principle effect of waves on delta development lies in delaying the initial time of formation (see Table 2). Broadly, this delay results from two distinct effects waves have on sediment transport: a first-order effect of wave-bed interaction, which increases magnitudes of both suspended load and bedload transport; and a second-order effect of transport resulting from currents induced by wave energy dissipation. At the discharging mouths of channels, sediments are transported further past the river mouth into the basin due to the former effect (either delaying or preventing mouth bar formation), but are also ultimately deflected landward by the latter. This is a complex interaction, with outcomes depending on local depths, currents, wave heights, and the orientation of discharging channels with respect to the direction (and spread) of waves. The strength of these effects depends primarily on the height of the incoming waves; under increasing H_s, the fully submerged margins of the sediment mass become larger in area, and sediments deposited in this region are distributed more evenly (compare Figures 6a, 6f, 6k, 6p, 6u, and 6z). Under the largest waves simulated ($H_s = 2.0$ m), alongshore spreading of sediments is also noticeably enhanced (larger σ_x—Figure 7f). The strength of this wave-driven sediment reworking effect is also evidenced by the larger $\langle \chi \rangle$ values seen under increasing H_s (Figure 7a). As sediment input Q_{sed} is identical between all simulations, wider alongshore spreading represented by σ_x also implies a reduction in overall bed elevations, which is indeed evident in the reduced centroid heights in comparison to increased σ_x values for larger waves seen in Figures 7e and 7f respectively. Simulations W0.0T0.0 to W1.2T0.0 (Figures 6a, 6f, 6k, and 6p) all produce quite large values for $\langle \chi_{inner} \rangle$, $\langle c_{split} \rangle$, and $\langle c_{mob} \rangle$. We classify such deltas as "river-controlled".

At the highest H_s values modeled without tides—simulations W1.6T0.0 (Figure 6u) and W2.0T0.0 (Figure 6z)—$\langle \chi \rangle$ increases greatly in comparison to the smaller H_s simulations (Figure 7a), and a different regime of morphological development is established. This regime involves the initial formation of coastline-adjacent emergent regions to either side of the river mouth with a wide estuarine region forming centrally, which then transitions to a delta as the estuary infills with sediment (see Section 4.1.3). We classify deltas forming in this way as "wave-controlled".

Tides without waves show no inhibiting effect on delta formation. In all such simulations, a delta forms within 3 years (see Table 2). Introduction of tides induces a modest decrease in both $\langle c_{split} \rangle$ and $\langle c_{mob} \rangle$ (Figures 7c and 7d) in comparison to W0.0T0.0. Excess mobility number $\langle \chi \rangle$ also initially reduces as H_t increases, but then rises

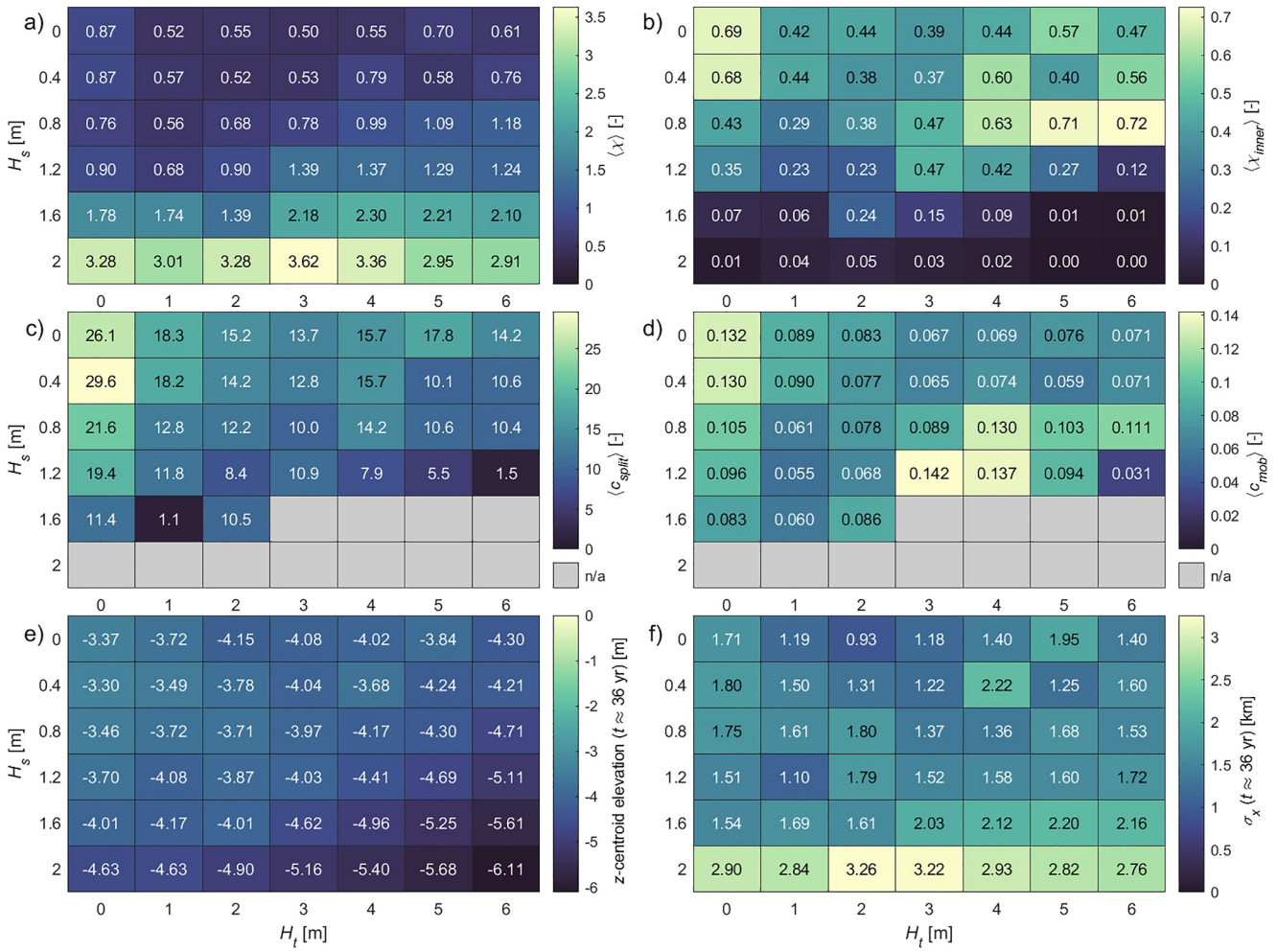

Figure 7. Heat-maps of all morphodynamic metrics up to $t \approx 36$ yr for all simulations: (a) 0–36 years temporal means of χ; (b) 0–36 years temporal means of χ_{inner}; (c) temporal means of instantaneous c_{split}; (d) temporal means of c_{mob}; (e) z-centroid elevations with respect to MSL at $t \approx 36$ yr; and (f) σ_x values at $t \approx 36$ yr. Note that both channel split counts and channel mobility numbers and means are calculated only from the point of delta formation up to $t \approx 36$ yr. Gray blocks in (c) and (d) are those for which no data exists, as deltas (and hence delta channels) did not form within the ~36 yr period covered.

slightly again under larger tides (H_t = 5 m and 6 m—Figure 7a). This reflects an initial stabilizing effect of increasing H_t followed by a cycle of sediment deposition and remobilization within the channel network as tidal discharges become larger. Where tides have this stabilizing effect on the channel network, we classify delta development as "river/tide-controlled".

When including waves alongside tidal variation, the cyclical vertical "sweep" of tides combines with the sediment transporting effects of waves (both wave-induced stirring and currents induced by wave energy dissipation), leading to a pattern of deposition and subsequent remobilization of sediments throughout the intertidal zone, both within and between channels. This is reflected by the higher $\langle\chi\rangle$ values seen under larger combinations of H_t and H_s in Figure 7a. Broadly, this combination of waves and tides causes a wider spread of sediments and related lowering of bed elevations, evident in the lower z-centroids and increased σ_x values seen in Figures 7e and 7f as well as in, for example, the morphologies seen in Figures 6e, 6j, 6o, 6t, 6y, and 6ad. At the highest combinations of H_s and H_t—e.g. simulations W1.6T6.0, W2.0T2.0, W2.0T4.0, and W2.0T6.0 (Figures 6y, 6ab, 6ac, and 6ad respectively)—this inhibiting effect is large enough to prevent the formation of persistent deposits above low tide, and hence prevent delta formation from occurring within ~72 yr. This critical finding suggests that delta formation may indeed be prevented from occurring under sufficiently energetic marine conditions. We classify regimes in which delta formation is prevented as "wave/tide-suppressed".

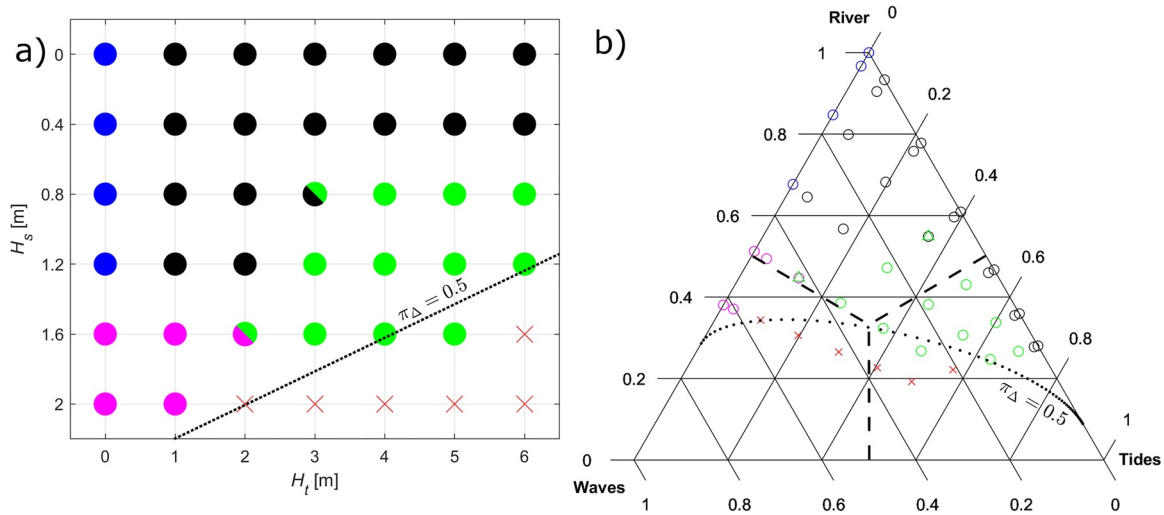

Figure 8. Delta regimes: magenta are wave-controlled; blue are river-controlled; black are river/tide-controlled; green are wave/tide-controlled; marks with two colors are unclear cases which lie between other regimes; red crosses are wave/tide-suppressed. Black dotted lines show the delimiting line between delta formation being considered likely or unlikely according to Equation 1 (Caldwell et al., 2019), while maintaining $\langle Q_0 \rangle = 1280$ m^{3}s^{-1} and $\langle Q_{sed} \rangle = 0.048$ m^{3}s^{-1}. Presented are the classification of regimes by (a) H_s and H_t; and (b) the methodology of Nienhuis et al. (2015); Nienhuis et al. (2018, 2020) (this subplot produced in part using MATLAB code by Rik, 2024). Note that the relative influences in (b) are determined following the methodology of Nienhuis et al. (2015); Nienhuis et al. (2018, 2020), using input parameters from the respective simulations rather than fluxes determined from simulation data. The MATLAB functions/scripts used to make these calculations are freely available online (see Open Research Section). By Nienhuis's definitions, points in the lower left section are wave-dominated, lower right section are tide-dominated, and upper section are river-dominated. These sections are delimited by dashed black lines.

While combinations of the largest H_s and H_t modeled prevented deltas from forming, a further distinct regime of delta formation occurs at intermediate combinations—e.g. W0.8T4.0, W0.8T6.0, and W1.2T4.0 (Figures 6n, 6o, and 6s). In these simulations, marine conditions are not quite sufficient to prevent delta formation, but they are sufficient to provide the energy needed for morphology to remain highly active throughout the deposited sediment mass. This effect is evident in the quite high $\langle \chi \rangle$ values, very high $\langle \chi_{inner} \rangle$ values, and very high $\langle c_{mob} \rangle$ values (Figures 7a, 6c and 7d respectively) seen for simulations W0.8T4.0, W0.8T5.0, W0.8T6.0, W1.2T3.0, and W1.2T4.0. We classify delta development of this type as "wave/tide-controlled." Note that we also classify simulations W1.2T5.0, W1.2T6.0, W1.6T3.0, W1.6T4.0, and W1.6T5.0 as wave/tide-controlled (see Section 4.1), despite these simulations not having values of morphodynamic metrics as described above. This is due to these latter simulations only forming deltas close to, or in some cases after, 36 years. As such, the processes described are only briefly observed, if at all, within the 36 years window covered by the morphodynamic analysis.

4. Discussion

4.1. Delta Formation Regimes and Development Processes

Several distinct regimes of delta development were identified in Section 3. Each simulation is categorized by regime in Figure 8a, based on their observed, qualitative development over time, as well as values of morphodynamic metrics in Figure 7. Additionally, Figure 8b plots the simulations according to the process-dominance framework of Nienhuis et al. (2015); Nienhuis et al. (2018, 2020). Black dotted lines on Figures 8a and 8b show the dividing line between delta formation being likely or unlikely according to Equation 1 (i.e., $\pi_\Delta = 0.5$) (Caldwell et al., 2019). This line proves to be remarkably accurate in identifying the threshold between the delta-forming and non-delta-forming simulations.

While there is a loose correspondence between our defined regimes and the wave/tide/river-dominated classifications according to Figure 8b, some notable differences are apparent. Most significantly, we classify several simulations as river/tide-controlled, and some simulations as wave/tide-controlled, which fall within the river-dominated classification of Figure 8b. By way of explanation, we first note that process-dominance according to the methodology of Nienhuis et al. (2015); Nienhuis et al. (2018, 2020) is determined via a characteristic sediment transport associated with river discharge, tidal prism, or alongshore wave transport, each of which are treated independently. By contrast, our own regime classifications follow the semi-quantitative analysis presented

in this Section, for which the interaction between processes also has a significant effect on morphodynamic development—tides in particular have a greater effect on formational processes resulting from the interaction between water level variation and river discharge/wave-driven transport, than directly resulting from the transportive capacity of the tidal prism.

We also note that none of our simulations are defined as purely tide-controlled, as we generally found that it is this interaction of tides with other processes which controls the mechanisms of delta development. We acknowledge, however, that the local geological setting might also affect the relative importance of tidal effects. Here, we have modeled delta formation in an open coastal setting; however, deltas forming within a laterally constrained, "drowned river valley" environment, might exhibit developmental processes with a more explicit tidal morphological signature (such as described by, e.g. Galloway, 1975; Orton & Reading, 1993). While we believe that the effort to define quantitative, deterministic measures of the influence of these primary processes on delta formation (or inhibition) is a reasonable one, we suggest that such quantification might be improved by deriving characteristic transport equations which take process interaction into account.

Based on developmental laws outlined by Wolinsky et al. (2010), we expect that deltas in the river- and river/tide-controlled regimes would exhibit similar ongoing development were their durations to be extended beyond 36 years. At larger wave heights—particularly in the wave/tide-controlled regime—delta development matches these laws less clearly, hence the nature of continuing development beyond the durations modeled is less clear for these regimes (see Text S4 in Supporting Information S1).

Qualitative comparison between our simulations and real-world examples for each of our proposed delta (non-) formation regimes can be found in Text S5, Figure S4, and Table S2 of Supporting Information S1.

4.1.1. River-Controlled Delta Formation

In river-controlled simulations, a mouth bar first forms within the discharging jet of the initial river mouth, leading to channel bifurcation and formation of a delta within 3–8 years (see e.g. supplementary Movie S1 for simulation W0.8T0.0). Continuing delta growth is characterized by a combination of mouth-bar induced bifurcation at channel tips, as well as frequent avulsions where channels overtop their banks. The high $\langle\chi\rangle$ and $\langle c_{split}\rangle$ are indicative of how the avulsion process interacts with the overall very flat elevations of delta plains for these cases; where avulsions occur, they lead to an initial period of shallow overland flow over the flat delta plain. This flow subsequently resolves into multiple small channels, many of which quickly become inactive (Hoyal & Sheets, 2009). The slight reduction in $\langle c_{split}\rangle$ and $\langle c_{mob}\rangle$ from simulation W0.0T0.0 to W1.2T0.0 (Figures 7c and 7d) is a consequence of both slower channel growth due to broader distribution of sediment by waves at channel ends (Ratliff et al., 2018), and also of the inhibiting effects of waves on mouth bar formation; this results in fewer channel splits as a result of mouth-bar induced bifurcation (Gao et al., 2018; Jerolmack & Swenson, 2007). Avulsion frequency is also reduced by slowing of mouth bar formation, as avulsion occurs primarily as a consequence of upstream-propagating effects of mouth bar formation on both hydro- and morphodynamics (Edmonds et al., 2009; Hoyal & Sheets, 2009).

4.1.2. River/Tide-Controlled Delta Formation

In contrast to purely river-controlled deltas, river/tide-controlled deltas have comparatively low $\langle\chi\rangle$, $\langle c_{split}\rangle$, and $\langle c_{mob}\rangle$ values (Figures 7a, 7c and 7d). Simulations with $H_s \leq 0.8$ m have surface elevations ranging from around high tide water level close to the delta apex (here defined as the midpoint of the initial river mouth), down to (by definition) the low tide water level. This leads to steeper overall delta plain gradients under increasing values of H_t (compare Figures 6a–6e and 6f–6j). This affects the process of overland flow resolving into multiple channels as described by Hoyal and Sheets (2009), with avulsions appearing less frequent as H_t increases, resulting in the formation of fewer channels.

Compared to non-tidal simulations, tides also form deeper and wider deltaic channels, and also maintain (rather than infill) both active and inactive channels (Broaddus et al., 2022; Iwantoro et al., 2020; Rossi et al., 2016; Zhou et al., 2020), which in part explains the reduction in $\langle\chi\rangle$ and $\langle c_{mob}\rangle$. We observe no clear, quantifiable change in mouth-bar induced bifurcation frequency for these simulations, with the majority of reduction in both $\langle c_{mob}\rangle$ and $\langle c_{split}\rangle$ (see top two rows in Figures 7c and 7d) apparently due primarily to the discussed reduction in avulsion frequency. Differences discussed in this section can be seen by comparison of

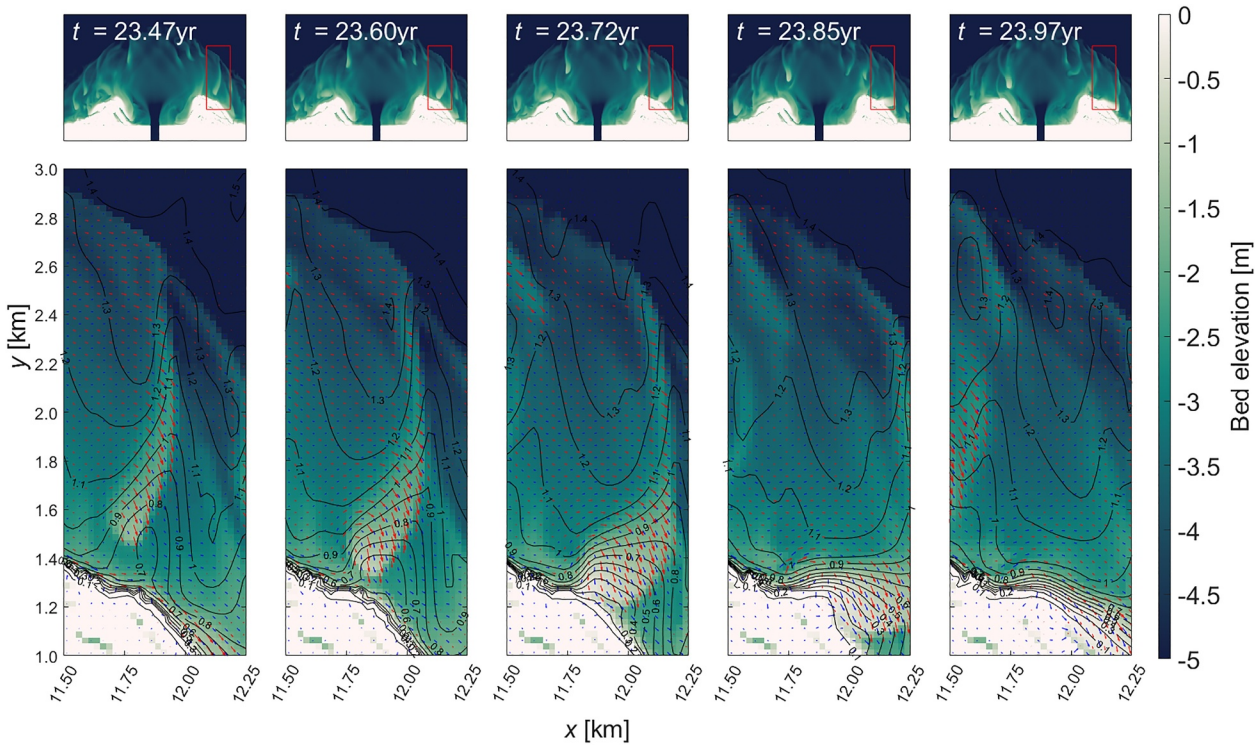

Figure 9. Time-series showing shore-normal bar migration and beaching for simulation W2.0T0.0. Bathymetry shown with: depth-averaged current vectors (blue arrows, shown at intersections of odd-numbered cells only); sediment transport vectors for total load (red arrows, shown at intersections of odd-numbered cells only); and labeled contours of H_s. Vector lengths are indicative of relative magnitude of their respective quantities only.

supplementary Movie S1 and Movie S2 showing bathymetry over time for, for example, simulations W0.0T0.0 and W0.0T5.0.

4.1.3. Wave-Controlled Delta Formation

Wave-controlled delta formation in our simulations does not result from the processes of mouth-bar induced bifurcation and avulsion by which delta formation is typically explained. Instead, wave-controlled delta formation is characterized by development of an estuarine region which narrows to form a delta. This is a complex process which occurs as follows: mouth bar formation close to the river mouth is prevented by the higher-energy waves, with sediments transporting further past the river mouth to initially form a broad submerged fan. Within this fan, we see the formation of transverse (approximately shore-normal) bars with peak elevations at, or just below, the local water surface. Figure 9 shows an example of the development over time of one of these bars in simulation W2.0T0.0. Note the reduction in H_s from the offshore end of the bar to the nearshore end; this reduction indicates the dissipation of wave energy occurring along the bar, which translates into the observed shoreward-deflection of currents and related sediment fluxes. This shoreward sediment flux leads to sediment accumulation at the initial coastline, resulting in the formation and subsequent growth of the emergent deposits on either side of the river mouth, with a wide estuarine region forming centrally.

As the estuarine region grows over time, some of the bars beginning to form near the midline of the discharging jet are transported back into the estuary, rather than along the outer edges of the flanking deposits. An example of this process is represented in Figure 10. Here we see the shoreward end of a nascent bar spreading laterally to form a ridge normal to the mean incident wave direction. As the crest of the bar rises closer to the local water level, water currents and related sediment fluxes are diverted around the sides of the crest rather than over it. The resultant circulation around either side of the crest (Figure 10 panels 2 and 3) is enhanced by wave dissipation-induced currents on the up-wave side of the crest. The combined effect is that the forces driving this bar inward now exceed forces driving it outward, and the bar travels into the estuary, where it eventually stagnates (panel 5 of

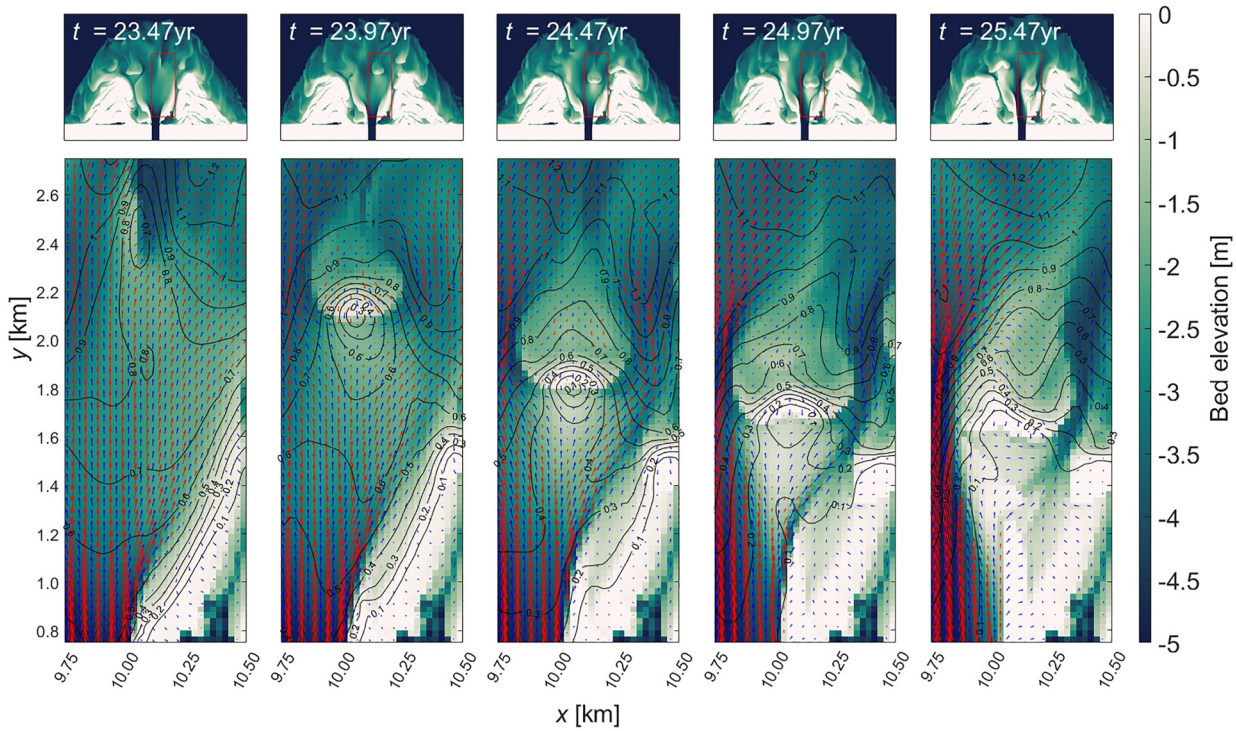

Figure 10. Time-series showing the process of bar transport into the estuary leading to estuarine infilling and transition to deltaic morphology for simulation W1.6T0.0. Bathymetry shown with: depth-averaged current vectors (blue arrows, shown at intersections of odd-numbered cells only); sediment transport vectors for total load (red arrows, shown at intersections of even-numbered cells only); and labeled contours of H_s. Vector lengths are indicative of relative magnitude of their respective quantities only.

Figure 10). Repeated instances of this process lead to narrowing of the wide estuary toward a narrow channelized configuration, marking a transition from an open estuarine morphology toward a deltaic one.

While the idealized, steady boundary nature of the simulations may mean that the above-described process is not necessarily observable in reality, this development process does represent a potential novel mechanism of delta and estuary formation. This may have repercussions with respect to, for example, interpretation of the stratigraphic rock record where conducting field investigations into the development of deltaic and estuarine systems in historically micro-tidal, high wave energy regions.

4.1.4. Wave/Tide-Controlled Delta Formation

Wave/tide-controlled delta formation is marked by high values of $\langle\chi\rangle$, $\langle\chi_{inner}\rangle$, and $\langle c_{mob}\rangle$, but with lower $\langle c_{split}\rangle$ in comparison to river-controlled deltas (Figures 7a–7d). Most notably, the processes of mouth-bar induced bifurcation and, particularly, channel avulsion are less clearly observed in these cases. This is attributed to the high mobility of sediments throughout the delta, both inside and between channels. Mouth bars in these simulations shift their position over time alongside the highly mobile channels. This contrasts sharply with the relative immobility of such features when unaffected by either waves or tides; prior studies have demonstrated that, in such cases, mouth bars adopt an approximately fixed position once water depth at their crests reduces to a particular ratio (depending on local basin slope) relative to the surrounding local water depth (Edmonds & Slingerland, 2007; Jiménez-Robles et al., 2016). Avulsions, which were easily observable in lower marine-energy simulations, are still evident, but the combined processes controlling their development in these cases are difficult to disentangle.

4.1.5. Wave/Tide-Suppression of Delta Formation

Wave/tide-suppression of delta formation occurs when waves and tides in combination act to severely limit persistent deposits from accreting above the low tide water level. Simulations in which these conditions occurred

are marked by alongshore bar transport oriented away from the discharging river mouth. While these bars are at times emergent, such emergence is typically short-lived, with bar crests returning to a fully submerged level as they travel alongshore. The movement of these bars is as described in Section 4.1.3, but marine conditions are such that accumulation of persistent emergent regions to either side of the discharging river no longer occurs.

4.2. Wave and Tide Driven Sediment Diffusion as a Mechanism for Inhibition of Delta Growth

While sediment transport is actually in part diffusive and in part advective, it is argued here that the overall pattern of spreading under combined tidal variation and larger waves may be well approximated by a simple diffusive transport equation. We assume that sediment transport and bed elevation change can be described by an Exner (1925) equation of form:

$$\xi \frac{\partial z_b}{\partial t} = -\left\{\frac{\partial q_x}{\partial x} + \frac{\partial q_y}{\partial y}\right\} + D - E \tag{2}$$

where z_b is bed elevation [m]; q_x, q_y are sediment fluxes per meter width in the x and y directions respectively [m^2s^{-1}]; D (E) is deposition (erosion) rate per unit area [ms^{-1}]; and $\xi = 1 - n$ is a factor allowing for void-space in the bed [-]. For the large tidal ranges considered, sediment discharging from the river is generally deposited to the bed within the tidal cycle during which it enters. From that point onward, deposition and erosion of sediment remain in approximate equilibrium, as bed sediments are cyclically deposited and remobilized over successive tides. We hence simplify the analysis by stating that $D \equiv E$, thus eliminating those terms from Equation 2. We also assume all subsequent sediment transport can be represented simply by the sediment flux terms q_x and q_y in Equation 2, regardless of the actual mechanisms of transport—i.e. whether as bedload or suspended load. Integrating Equation 2 in the cross-shore (y) direction:

$$\xi \int_0^{L_y} \frac{\partial z_b}{\partial t} dy = \frac{\partial V}{\partial t} \qquad \text{where } V(x,t) = \xi \int_0^{L_y} z_b(x,y,t)\, dy$$

is the total volume of river-delivered sediment per meter alongshore [m^2];

$$\int_0^{L_y} \frac{\partial q_x}{\partial x} dy = \frac{\partial Q}{\partial x} \qquad \text{where } Q(x,t) = \int_0^{L_y} q_x(x,y,t)\, dy; \text{ and}$$

$$\int_0^{L_y} \frac{\partial q_y}{\partial y} dy = q_y(x, L_y, t) - q_y(x, 0, t) = -q_y(x, 0, t),$$

Equation 2 becomes:

$$\frac{\partial V}{\partial t} = -\frac{\partial Q}{\partial x} + q_y(x, 0, t). \tag{3}$$

Observing that the overall movement of bed sediments in such simulations is typically alongshore away from the river mouth, we assume that we can state $Q = -\kappa(x,t)\frac{\partial V}{\partial x}$, where κ is a coefficient of diffusion [m^2s^{-1}]. This means that sediment will move down its own alongshore gradient, driven by gravity but also aided (or hindered) by additional agitation resulting from waves and currents. The coefficient κ can hence be viewed as quantifying the strength of this downslope sediment transport. It follows that Equation 3 may be written as:

$$\frac{\partial V}{\partial t} = \frac{\partial}{\partial x}\left\{\kappa(x,t)\frac{\partial V}{\partial x}\right\} + q_y(x, 0, t) \tag{4}$$

where $q_y(x, 0, t) = Q_{sed}/W$ for $0.5(L_x - W) \le x \le 0.5(L_x + W)$ or $q_y(x, 0, t) = 0$ m^2s^{-1} otherwise; W is the width over which incoming sediment flux Q_{sed} is distributed [m]; and L_x is the alongshore width of the domain [m]. Notionally κ represents a spatially and temporally varying alongshore bed diffusion coefficient, which is unknown. In contrast, W notionally represents the river width, which is fixed here and known. As a practical

Table 3
Values of κ, W, and Related RMSE for All Wave-Controlled, Wave/Tide-Controlled, and Wave/Tide-Suppressed Simulations

H_s [m]	H_t [m]	Regime	κ [m^2s^{-1}]	W [m]	RMSE [m^3m^{-1}]
0.8	3.0	RT/WT	0.0020	4,250	7,022
	4.0	WT	0.0025	4,000	7,678
	5.0	WT	0.0025	4,000	6,695
	6.0	WT	0.0025	4,250	7,334
1.2	3.0	WT	0.0025	4,250	5,123
	4.0	WT	0.0025	4,500	4,949
	5.0	WT	0.0025	4,500	5,054
	6.0	WT	0.0030	4,500	5,035
1.6	0.0	W	0.0025	4,500	5,525
	1.0	W	0.0030	4,250	5,025
	2.0	W/WT	0.0025	4,750	7,118
	3.0	WT	0.0035	5,000	4,586
	4.0	WT	0.0040	5,000	5,794
	5.0	WT	0.0040	5,000	5,148
	6.0	X	0.0040	5,000	4,623
2.0	0.0	W	0.0075	5,000	3,139
	1.0	W	0.0070	4,500	4,070
	2.0	X	0.0095	5,250	4,810
	3.0	X	0.0090	5,750	4,349
	4.0	X	0.0070	5,750	3,930
	5.0	X	0.0065	5,500	4,194
	6.0	X	0.0060	5,500	3,745

Note. W denotes wave controlled; WT denotes wave/tide controlled; X denotes wave/tide suppressed; RT/WT denotes mixed river/tide and wave/tide controlled; and W/WT denotes mixed wave and wave/tide controlled.

measure, we here set κ to be constant, which is to be fitted to the simulation data. To allow for the probable locally higher rates of diffusion in the vicinity of the river outflow, we also regard W as a fitting parameter. This is accordingly best viewed as representing the distributive capacity of the discharging jet of the river, which spreads sediments far beyond the vicinity of the river mouth independently of any additional diffusion resulting from wave/tide-induced transport represented by κ. It therefore seems reasonable to anticipate that the best-fit W would be substantially larger than the actual river width.

We derive an approximate solution of Equation 4 (for constant κ) through the method of eigenfunction expansion (see e.g. Constanda, 2016): taking κ to be constant for all x and t, and defining initial conditions $V(x,0) = 0$ m^2 and Neumann boundary conditions $\frac{\partial V(0,t)}{\partial x} = 0$ m^2m^{-1} and $\frac{\partial V(L_x,t)}{\partial x} = 0$ m^2m^{-1}, we define:

$$V(x,t) = \sum_{n=0}^{\infty} f_n(t)\cos\left(n\pi\frac{x}{L_x}\right);\ \text{where} \tag{5}$$

$$f_n(t) = \begin{cases} t\dfrac{Q_{sed}}{L_x} & \text{for } n = 0 \\ \dfrac{\beta_n}{\alpha_n}[1 - \exp(-\alpha_n t)] & \text{for } n > 0; \end{cases} \tag{6}$$

and where $\alpha_n = \kappa\left(\frac{n\pi}{L_x}\right)^2$ and $\beta_n = \frac{2}{n\pi}\frac{Q_{sed}}{W}\left[\sin\left(\frac{n\pi}{2}\frac{L_x+W}{L_x}\right) - \sin\left(\frac{n\pi}{2}\frac{L_x-W}{L_x}\right)\right]$. We find this method to be convergent to unique solutions at values of n of $O(10)$, hence we apply it here in all cases with $n = 100$. Values of κ and W to be used in Equations 5 and 6 are determined—to the nearest 0.0005 m^2s^{-1} and 250 m respectively—using a least-squares fit approach over both x and t. We compared predictions made using Equations 5 and 6 to spatially and temporally smoothed bed level data (moving mean calculated over ±2 km in x and $\pm T_t/2$ in t—i.e. over one tide at hydrodynamic timescale), iterating to determine the smallest root mean square error (RMSE) possible.

Best-fit values of κ and W, as well as related RMSEs, are shown in Table 3 for all wave controlled, wave/tide controlled, and wave/tide suppressed simulations. Comparison between Delft3D data—for simulations W1.6T4.0, W1.6T6.0, W2.0T4.0, and W2.0T6.0—and predicted sediment distribution using Equation 5 is shown in Figure 11. We do not apply Equation 5 to either the river- or river/tide-controlled cases; simulations for which the assumptions underpinning the validity of the formula do not hold. Sediment distribution in such cases is controlled primarily by intrinsic mouth-bar and avulsion channel splitting processes rather than extrinsic transport due to tidal variation and waves associated with greater H_s and H_t. Generally, the accuracy with which Equation 5 matches the results of the Delft3D simulations increases with H_s, with the largest RMSEs in Table 3 occurring for simulations with $H_s = 0.8$ m and smallest RMSEs occurring for simulations with $H_s = 2.0$ m.

Broadly, values of W producing the closest fit for all non-delta forming simulations in Table 3 are ~5000–6000 m. Values of W reduce to around ~4000 m for simulations with $H_s = 0.8$ m, suggesting that waves contribute somewhat to the initial spread of river-delivered sediments, independently of any background alongshore transport. This makes physical sense, as wave-stirring acts to reduce rates of deposition within the river jet(s). As argued above, we expect that the magnitude of W relates primarily to the magnitude of river discharge; however, as we do not vary river discharge parameters in our simulations, we offer no definitive statement to that effect here.

Values of κ showed a dependence on H_s, with values as low as 0.002 m^2s^{-1} for simulations with $H_s = 0.8$ m, increasing to as high as 0.0095 m^2s^{-1} for simulations with $H_s = 2.0$ m. With the exception of simulations

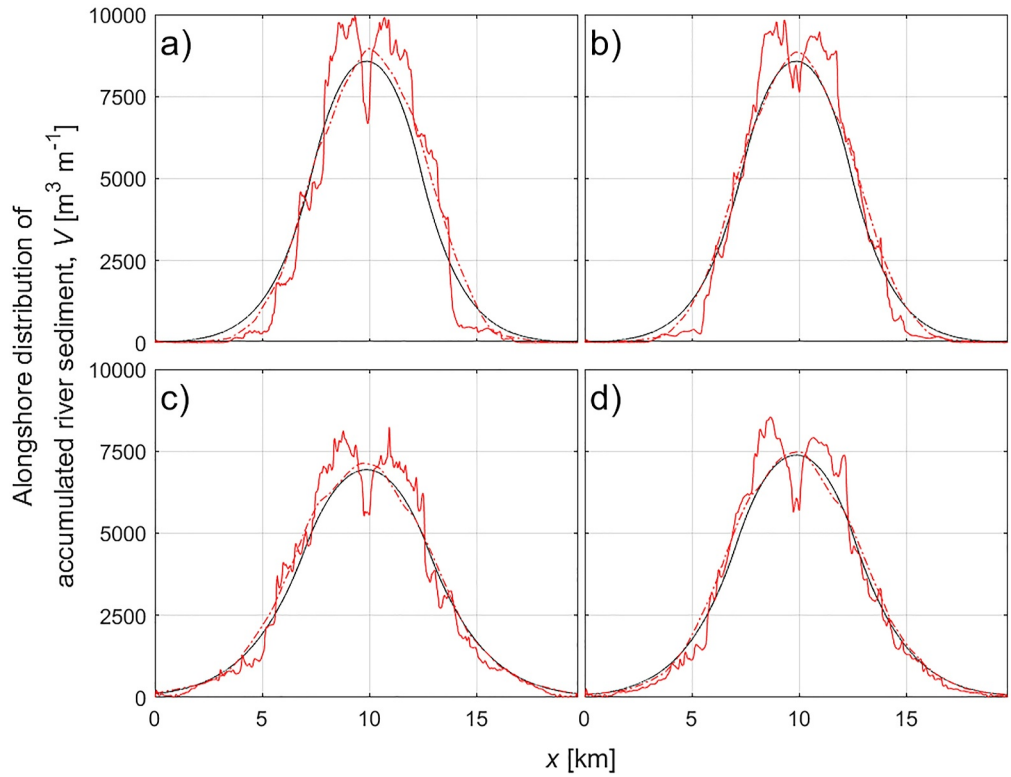

Figure 11. Plots of alongshore distribution of accumulated river sediment V (at $t \approx 36$ yr, for (smoothed) Delft3D simulation data in comparison to approximate solutions (Equation 5 with $n = 100$ and $L_x = 29750$ m). Black lines are approximate solutions, solid red lines are Delft3D simulation data, and dashed red lines are smoothed Delft3D data. Shown for: (a) W1.6T4.0 ($\kappa = 0.004$ m^{2}s^{-1}, $W = 5000$ m); (b) W1.6T6.0 ($\kappa = 0.004$ m^{2}s^{-1}, $W = 5000$ m); (c) W2.0T4.0 ($\kappa = 0.007$ m^{2}s^{-1}, $W = 5750$ m); and (d) W2.0T6.0 ($\kappa = 0.006$ m^{2}s^{-1}, $W = 5500$ m). (Note that x-coordinate shown relates to the convention of the Delft3D model; the x-coordinate of the analytical solution has been offset to match.)

W2.0T0.0 and W2.0T1.0, all delta-forming simulations had best-fit κ-values ≤ 0.004 m^{2}s^{-1}, suggesting $\kappa = 0.004$ m^{2}s^{-1} to be an appropriate first approximation as a lower boundary for the suppression of delta formation. We stress that this limit is not likely to be generalizable to all discharging river/basin systems, as it may well also depend on discharge parameters and (initial) coastal morphology, which were not varied here. In general, best-fit κ-values showed a slight increase with increasing H_t. However, this trend is not maintained for simulations with $H_s = 2.0$ m; here, κ reduces from a maximum 0.0095 m^{2}s^{-1} for simulation W2.0T2.0, down to 0.006 m^{2}s^{-1} for simulation W2.0T6.0. We attribute this effect to the tendency for larger H_t simulations to initially deposit sediments further offshore, as a result of faster ebb-tide currents (compare Figures 6ab–6ad). Sediments deposited further offshore due to this effect are subject to reduced wave-driven remobilization (as represented by excess mobility χ—Figure 7a), hence the observed reduction in κ. As a final note regarding κ, we also estimated diffusion coefficients for the analogous (wave-driven) shoreline diffusion equation (see e.g. Kamphuis, 2010, and Text S6 in Supporting Information S1). The coefficients determined in this analysis were: 0.0017 m^{2}s^{-1} at $H_s = 0.8$ m; 0.0029 m^{2}s^{-1} at $H_s = 1.2$ m; 0.0040 m^{2}s^{-1} at $H_s = 1.6$ m; and 0.0052 m^{2}s^{-1} at $H_s = 2.0$ m, which are broadly similar to those in Table 3.

Finally, we note that while Equation 5 was derived with delta non-formation cases in mind, it also performed well in replicating sediment distribution in the wave/tide-controlled and wave-controlled cases. Although RMSEs for the wave-controlled cases were amongst the lowest measured, we expect that Equation 5 would prove less accurate if applied to those simulations over longer durations; following the onset of delta formation in those cases, sediment distribution would, we expect, become increasingly determined by intrinsic (channel migration and avulsion-driven) rather than extrinsic (wave- and tide-driven) processes. The accuracy of Equation 5 with respect to future development of wave/tide-controlled cases is less clear, as the projected balance of intrinsic and extrinsic

Table 4
Magnitude of Morphodynamic Metrics Indicating Delta Regime

	$\langle\chi\rangle$	$\langle\chi_{inner}\rangle$	$\langle c_{split}\rangle$	$\langle c_{mob}\rangle$	z-centroid[a]	σ_x
River-controlled	Moderate	High	High	High	High	-
River/tide-controlled	Low	Moderate	Moderate	Moderate	-	-
Wave/tide-tide-controlled[b]	High	High	-	High	-	-
Wave-controlled	High	Low	-	-	Low	High
Wave/tide-suppressed	High	Low	-	-	Low	High

[a]Here, "Low" and "High" relate to the absolute elevation of the z-centroid. [b]These values are not reflected in all such simulations in Figure 7, due to the late formation of deltas in these cases as compared to the 36 years period over which metrics were evaluated.

drivers is harder to predict in such cases. This is in contrast to the expected development from primarily extrinsic to primarily intrinsic for the wave-controlled cases.

5. Conclusions

In this study, we investigated whether delta formation could be suppressed by sufficiently large values of significant wave height H_s, and tidal range H_t. In doing so, we modeled larger combinations of these parameters than have typically been modeled in previous studies. We identify four regimes of delta formation: river-controlled; river/tide-controlled; wave-controlled; and wave/tide-controlled. A fifth regime, wave/tide-suppression of delta formation, occurred under combinations of the largest H_s and H_t of those tested (up to 2 and 6 m respectively). We also compared our own classifications of process-control on delta formation to the prevailing process-dominance of Nienhuis et al. (2015); Nienhuis et al. (2018, 2020), suggesting that their process-dominance framework might be improved by consideration of process interaction, especially as concerns tides. Higher wave and tidal energy regimes—that is, wave-controlled and wave/tide-controlled formation regimes as well as wave/tide-suppression of delta formation—notably did not clearly exhibit the processes of mouth-bar induced bifurcation and avulsion by which delta development under smaller waves and tidal ranges is often characterized (e.g., Edmonds & Slingerland, 2010). Simulations designated here as wave-controlled do approximately match descriptions of strongly wave-affected "cuspate" delta growth models described in some prior studies (e.g., Ashton & Giosan, 2011; Dominguez, 1996; Komar, 1973), but diverge from these studies in that they also exhibit an early formational phase wherein an initially wide estuarine region narrows to a single channel; a potentially novel formational process with repercussions for interpretation of the geological record. The approximate magnitude of morphodynamic metrics associated with each regime is shown in Table 4 (dashes indicate that a particular morphodynamic metric is unimportant in identifying given regime).

We also identify the mechanisms by which waves and tides can potentially prevent delta formation altogether, finding agreement with the predictions of Caldwell et al. (2019). In such cases, a diffusion equation with source term can be used to fairly accurately predict the alongshore spreading of sediment. We suggest that Equation 4 is viable for predicting alongshore transport of discharging river sediment under approximately normally incident, high-energy waves, at coasts which do not form deltas, and also for those that form wave/tide-controlled deltas (by our proposed definitions). Such coastlines are often smooth and approximately straight (Anthony, 2015; Ratliff et al., 2018) (see also Figure S4j in Supporting Information S1), and hence are reasonably well represented by our idealized model. While it is outside the scope of this paper to do so, it seems plausible that κ and W in Equation 5 might be explicitly defined as functions of H_s, wave spreading, mean wave direction, Q_0, and Q_{sed}. As a first approximation, a value of $\kappa = 0.004$ m^2s^{-1} is suggested as a boundary between delta formation and non-formation.

It is reasonable to wonder if delta formation would continue to be prevented over longer durations than modeled here, and for conditions other than those considered here. We suggest that a more complete analysis would thoroughly consider the processes by which sediment is transported far from the river mouth, beyond the depositional region of the potential delta. This might occur under several conditions: where mean wave directions are not directly shore-normal, thus inducing ongoing littoral drift; where tidal asymmetry is significant; where tides and other oceanic processes induce alongshore currents sufficient to transport sediments away from the local

depositional region; or even where sediments are transported as far as the continental shelf edge and are hence deposited into deep sea environments.

The description of lateral spreading of sediment embodied in Equation 4 has a potential practical use in, for instance, the prediction of the possible effect of restricting sediment output due to upstream damming. If W and κ can be related to waves, tides and river discharge, then Equation 4 can constitute the basis for an efficient method for determining the threshold for delta stagnation or destruction.

Data Availability Statement

Build 69,179 of Delft3D 4, used for all simulations, is available from https://svn.oss.deltares.nl/repos/delft3d/tags/delft3d4/69179/, distributed under a GNU lesser general public license, and developed openly at https://oss.deltares.nl/web/delft3d. The simulation input and output files, and animations of all simulations are available at the British Oceanographic Data Centre (BODC), under a UK Open Government License v3.0 (Sloan et al., 2024). MATLAB scripts used for generating some input files, analyzing data, and generation of figures/animations are available online, under a Creative Commons Attribution 4.0 International license (Sloan, 2024).

Acknowledgments
We thank the Natural Environment Research Council and Envision DTP for funding the studentship which facilitated this work (Grant reference NE/S007423/1, project reference 2435809). Comments and suggestions offered by Connor Broaddus and two anonymous reviewers helped to greatly strengthen this manuscript, and we thank them for their time and insight. Additionally, we would like to thank Anurak Sriariyawat of Chulalongkorn University Department of Water Resource Engineering for additional support, feedback, and comments. This study would not have been possible at all without use of the University of Nottingham High Performance Computer, and the assistance of Colin Bannister in installing the necessary software. Finally, the help of Matthew Appleton in developing MATLAB code to apply the opening angle method is gratefully acknowledged.

References

Anthony, E. J. (2015). Wave influence in the construction, shaping and destruction of river deltas: A review. *Marine Geology*, *361*, 53–78. https://doi.org/10.1016/j.margeo.2014.12.004

Ashton, A. D., & Giosan, L. (2011). Wave-angle control of delta evolution. *Geophysical Research Letters*, *38*(13). https://doi.org/10.1029/2011GL047630

Athanasiou, P., van Dongeren, A., Giardino, A., Vousdoukas, M., Gaytan-Aguilar, S., & Ranasinghe, R. (2019). Global distribution of nearshore slopes with implications for coastal retreat. *Earth System Science Data*, *11*(4), 1515–1529. https://doi.org/10.5194/essd-11-1515-2019

Baar, A., Boechat Albernaz, M., Van Dijk, W., & Kleinhans, M. (2019). Critical dependence of morphodynamic models of fluvial and tidal systems on empirical downslope sediment transport. *Nature Communications*, *10*(1), 4903. https://doi.org/10.1038/s41467-019-12753-x

Bird, E. (2008). *Coastal geomorphology: An introduction*. Wiley. Retrieved from https://books.google.co.uk/books?id=-YX0mWBpjGkC

Broaddus, C. M., Vulis, L. M., Nienhuis, J. H., Tejedor, A., Brown, J., Foufoula-Georgiou, E., & Edmonds, D. A. (2022). First-order river delta morphology is explained by the sediment flux balance from rivers, waves, and tides. *Geophysical Research Letters*, *49*(22), e2022GL100355. https://doi.org/10.1029/2022GL100355

Burpee, A. P., Slingerland, R. L., Edmonds, D. A., Parsons, D., Best, J., Cederberg, J., et al. (2015). Grain-size controls on the morphology and internal geometry of river-dominated deltas. *Journal of Sedimentary Research*, *85*(6), 699–714. https://doi.org/10.2110/jsr.2015.39

Caldwell, R. L., & Edmonds, D. A. (2014). The effects of sediment properties on deltaic processes and morphologies: A numerical modeling study. *Journal of Geophysical Research: Earth Surface*, *119*(5), 961–982. https://doi.org/10.1002/2013JF002965

Caldwell, R. L., Edmonds, D. A., Baumgardner, S., Paola, C., Roy, S., & Nienhuis, J. H. (2019). A global delta dataset and the environmental variables that predict delta formation on marine coastlines. *Earth Surface Dynamics*, *7*(3), 773–787. https://doi.org/10.5194/esurf-7-773-2019

Constanda, C. (2016). *Solution techniques for elementary partial differential equations* (3rd ed.). Taylor and Francis Group. https://doi.org/10.1201/9781315381442

Deltares. (2021a). Delft3d hydro-morphodynamics user manual. [Computer software manual]. https://content.oss.deltares.nl/delft3d4/Delft3D-FLOW_User_Manual.pdf

Deltares. (2021b). Delft3d wave user manual. [Computer software manual]. https://content.oss.deltares.nl/delft3d4/Delft3D-WAVE_User_Manual.pdf

Dominguez, J. (1996). The são francisco strandplain: A paradigm for wave-dominated deltas? *Geological Society, London, Special Publications*, *117*(1), 217–231. https://doi.org/10.1144/GSL.SP.1996.117.01.13

Edmonds, D. A., Caldwell, R., Brondízio, E., & Siani, S. (2020). Coastal flooding will disproportionately impact people on river deltas. *Nature Communications*, *11*(1), 1234567890. https://doi.org/10.1038/s41467-020-18531-4

Edmonds, D. A., Hoyal, D. C., Sheets, B. A., & Slingerland, R. L. (2009). Predicting delta avulsions: Implications for coastal wetland restoration. *Geology*, *37*(8), 759–762. https://doi.org/10.1130/G25743A.1

Edmonds, D. A., & Slingerland, R. L. (2007). Mechanics of river mouth bar formation: Implications for the morphodynamics of delta distributary networks. *Journal of Geophysical Research*, *112*(F2). https://doi.org/10.1029/2006JF000574

Edmonds, D. A., & Slingerland, R. L. (2010). Significant effect of sediment cohesion on delta morphology. *Nature Geoscience*, *3*(2), 105–109. https://doi.org/10.1038/ngeo730

Exner, F. M. (1925). *Über die wechselwirkung zwischen wasser und geschiebe in flüssen: Gedr*. mit unterstützg aus d. jerome u. margaret stonborough-fonds. Hölder-Pichler-Tempsky, A.-G.

Fox-Kemper, B., Hewitt, H., Xiao, C., Adalgeirsdóttir, G., Drijfhout, S., Edwards, T., et al. (2021). Ocean, cryosphere and sea level change [Book Section]. In V. Masson-Delmotte, et al. (Eds.), *Climate change 2021: The physical science basis. Contribution of working group i to the sixth assessment report of the intergovernmental panel on climate change* (pp. 1211–1362). Cambridge University Press. https://doi.org/10.1017/9781009157896.011

Frasson, R. P. d. M., Pavelsky, T. M., Fonstad, M. A., Durand, M. T., Allen, G. H., Schumann, G., et al. (2019). Global relationships between river width, slope, catchment area, meander wavelength, sinuosity, and discharge. *Geophysical Research Letters*, *46*(6), 3252–3262. https://doi.org/10.1029/2019GL082027

Galloway, W. E. (1975). *Process framework for describing the morphologic and stratigraphic evolution of deltaic depositional system* (Vol. 31, pp. 127–156). Society of Economic Paleontologists and Mineralogist (SEPM), Special Publication.

Gao, W., Nienhuis, J., Nardin, W., Wang, Z. B., Shao, D., Sun, T., & Cui, B. (2020). Wave controls on deltaic shoreline-channel morphodynamics: Insights from a coupled model. *Water Resources Research*, *56*(9), e2020WR027298. https://doi.org/10.1029/2020WR027298

Gao, W., Shao, D., Wang, Z. B., Nardin, W., Rajput, P., Yang, W., et al. (2019). Long-term cumulative effects of intra-annual variability of unsteady river discharge on the progradation of delta lobes: A modeling perspective. *Journal of Geophysical Research: Earth Surface*, *124*(4), 960–973. https://doi.org/10.1029/2017JF004584

Gao, W., Shao, D., Wang, Z. B., Nardin, W., Yang, W., Sun, T., & Cui, B. (2018). Combined effects of unsteady river discharges and wave conditions on river mouth bar morphodynamics. *Geophysical Research Letters*, *45*(23), 12–903. https://doi.org/10.1029/2018GL080447

Geleynse, N., Storms, J. E., Walstra, D.-J. R., Jagers, H. A., Wang, Z. B., & Stive, M. J. (2011). Controls on river delta formation; insights from numerical modelling. *Earth and Planetary Science Letters*, *302*(1), 217–226. https://doi.org/10.1016/j.epsl.2010.12.013

Geleynse, N., Storms, J. E. A., Stive, M. J. F., Jagers, H. R. A., & Walstra, D. J. R. (2010). Modeling of a mixed-load fluvio-deltaic system. *Geophysical Research Letters*, *37*(5). https://doi.org/10.1029/2009GL042000

Guo, L., Wegen, M., Roelvink, D. J., Wang, Z. B., & He, Q. (2015). Long-term, process-based morphodynamic modeling of a fluvio-deltaic system, part i: The role of river discharge. *Continental Shelf Research*, *109*, 95–111. https://doi.org/10.1016/j.csr.2015.09.002

Hoitink, A. J. F., Wang, Z. B., Vermeulen, B. F., Huismans, Y., & Kästner, K. (2017). Tidal controls on river delta morphology. *Nature Geoscience*, *10*(9), 637–645. https://doi.org/10.1038/ngeo3000

Hoyal, D., & Sheets, B. (2009). 04). Morphodynamic evolution of experimental cohesive deltas. *Journal of Geophysical Research*, *114*(F2). https://doi.org/10.1029/2007JF000882

Iwantoro, A., van der Vegt, M., & Kleinhans, M. (2020). Morphological evolution of bifurcations in tide-influenced deltas. *Earth Surface Dynamics*, *8*, 413–429. https://doi.org/10.5194/esurf-8-413-2020

Jerolmack, D. J., & Swenson, J. B. (2007). Scaling relationships and evolution of distributary networks on wave-influenced deltas. *Geophysical Research Letters*, *34*(23). https://doi.org/10.1029/2007GL031823

Jiménez-Robles, A., Ortega-Sánchez, M., & Losada, M. (2016). Effects of basin bottom slope on jet hydrodynamics and river mouth bar formation. *Journal of Geophysical Research: Earth Surface*, *121*(6), 1110–1133. https://doi.org/10.1002/2016JF003871

Kamphuis, J. W. (2010). *Introduction to coastal engineering and management* (2nd ed., Vol. 48). World Scientific. https://doi.org/10.1142/7021

Komar, P. (1973). Computer models of delta growth due to sediment input from rivers and longshore transport. *Geological Society of America Bulletin*, *84*(7), 2217. https://doi.org/10.1130/0016-7606(1973)84⟨2217:CMODGD⟩2.0.CO;2

Lageweg, W., & Slangen, A. (2017). Predicting dynamic coastal delta change in response to sea-level rise. *Journal of Marine Science and Engineering*, *5*(2), 24. https://doi.org/10.3390/jmse5020024

Leonardi, N., Canestrelli, A., Sun, T., & Fagherazzi, S. (2013). Effect of tides on mouth bar morphology and hydrodynamics. *Journal of Geophysical Research: Oceans*, *118*(9), 4169–4183. https://doi.org/10.1002/jgrc.20302

Liu, Y., Chen, H., Wang, J., Yang, S., & Chen, A. (2020). Numerical simulation for the effects of waves and grain size on deltaic processes and morphologies. *Open Geosciences*, *12*(1), 1286–1301. https://doi.org/10.1515/geo-2020-0196

Mangor, K., Drønen, N. K., Kærgaard, K. H., & Kristensen, S. E. (2017). Shoreline management guidelines. *DHI*.

Milliman, J. D., & Farnsworth, K. L. (2011). *River discharge to the coastal ocean: A global synthesis*. Cambridge University Press.

Nardin, W., & Fagherazzi, S. (2012). The effect of wind waves on the development of river mouth bars. *Geophysical Research Letters*, *39*(12). https://doi.org/10.1029/2012GL051788

Nardin, W., Mariotti, G., Edmonds, D., Guercio, R., & Fagherazzi, S. (2013). Growth of river mouth bars in sheltered bays in the presence of frontal waves. *Journal of Geophysical Research: Earth Surface*, *118*(2), 872–886. https://doi.org/10.1002/jgrf.20057

Nienhuis, J. H., Ashton, A. D., Edmonds, D. A., Hoitink, A., Kettner, A. J., Rowland, J. C., & Törnqvist, T. E. (2020). Global-scale human impact on delta morphology has led to net land area gain. *Nature*, *577*(7791), 514–518. https://doi.org/10.1038/s41586-019-1905-9

Nienhuis, J. H., Ashton, A. D., & Giosan, L. (2015). What makes a delta wave-dominated? *Geology*, *43*(6), 511–514. https://doi.org/10.1130/G36518.1

Nienhuis, J. H., Hoitink, A. J. F. T., & Törnqvist, T. E. (2018). Future change to tide-influenced deltas. *Geophysical Research Letters*, *45*(8), 3499–3507. https://doi.org/10.1029/2018GL077638

Orton, G. J., & Reading, H. G. (1993). Variability of deltaic processes in terms of sediment supply, with particular emphasis on grain size. *Sedimentology*, *40*(3), 475–512. https://doi.org/10.1111/j.1365-3091.1993.tb01347.x

Ratliff, K. M., Hutton, E. H. W., & Murray, A. B. (2018). Exploring wave and sea-level rise effects on delta morphodynamics with a coupled river-ocean model. *Journal of Geophysical Research: Earth Surface*, *123*(11), 2887–2900. https://doi.org/10.1029/2018JF004757

Rik. (2024). Triangleplot. MATLAB central file exchange. Retrieved from https://www.mathworks.com/matlabcentral/fileexchange/64996-triangleplot

Roelvink, D., & Reniers, A. (2011). *A guide to modeling coastal morphology* (Vol. 70). World Scientific. https://doi.org/10.1142/7712

Rossi, V., Kim, W., Leva Lopez, J., Edmonds, D., Geleynse, N., Olariu, C., et al. (2016). Impact of tidal currents on delta-channel deepening, stratigraphic architecture and sediment bypass beyond the shoreline. *Geology*, *44*(11), 927–930. https://doi.org/10.1130/G38334.1

Saito, Y., Chaimanee, N., Thanawat, J., & Syvitski, J. (2007). Shrinking megadeltas in Asia: Sea-level rise and sediment reduction impacts from case study of the Chao Phraya delta. *LOICZ Inprint*, *2007*, 3–9.

Seneviratne, S., Zhang, X., Adnan, M., Badi, W., Dereczynski, C., Di Luca, A., et al. (2021). Weather and climate extreme events in a changing climate [Book Section]. In V. Masson-Delmotte, et al. (Eds.), *Climate change 2021: The physical science basis. Contribution of working group i to the sixth assessment report of the intergovernmental panel on climate change* (pp. 1513–1766). Cambridge University Press. https://doi.org/10.1017/9781009157896.013

Shaw, J. B., Wolinsky, M. A., Paola, C., & Voller, V. R. (2008). An image-based method for shoreline mapping on complex coasts. *Geophysical Research Letters*, *35*(12). https://doi.org/10.1029/2008GL033963

Sloan, E. (2024). Manybears/delta-development-thresholds: Effects of tidal range and significant wave height on delta development - Matlab files v1.0.0 [Code]. *Zenodo*. https://doi.org/10.5281/zenodo.13385288

Sloan, E., Dodd, N., & Briganti, R. (2024). Idealised outputs on effects of tides and waves on delta development using the model delft3d on a 36 and 72 year scale. [Dataset]. NERC EDS British Oceanographic Data Centre NOC. https://doi.org/10.5285/19ab429a-b365-d9e9-e063-7086abc0c066

Syvitski, J., Anthony, E., Saito, Y., Zăinescu, F., Day, J., Bhattacharya, J. P., & Giosan, L. (2022). Large deltas, small deltas: Toward a more rigorous understanding of coastal marine deltas. *Global and Planetary Change*, *218*, 103958. https://doi.org/10.1016/j.gloplacha.2022.103958

Syvitski, J., & Saito, Y. (2007). Morphodynamics of deltas under the influence of humans. *Global and Planetary Change*, *57*(3), 261–282. https://doi.org/10.1016/j.gloplacha.2006.12.001

Syvitski, J., Vörösmarty, C. J., Kettner, A. J., & Green, P. (2005). Impact of humans on the flux of terrestrial sediment to the global coastal ocean. *Science (New York, N.Y.)*, *308*(5720), 376–380. https://doi.org/10.1126/science.1109454

Tejedor, A., Longjas, A., Caldwell, R., Edmonds, D. A., Zaliapin, I., & Foufoula-Georgiou, E. (2016). Quantifying the signature of sediment composition on the topologic and dynamic complexity of river delta channel networks and inferences toward delta classification. *Geophysical Research Letters*, *43*(7), 3280–3287. https://doi.org/10.1002/2016GL068210

van der Vegt, H., Storms, J., Walstra, D.-J., & Howes, N. (2016). Can bed load transport drive varying depositional behaviour in river delta environments? *Sedimentary Geology*, *345*, 19–23. https://doi.org/10.1016/j.sedgeo.2016.08.009

van Rijn, L. C. (1993). Principles of sediment transport in rivers, estuaries and coastal seas.

Wolinsky, M., Edmonds, D., Martin, J., & Paola, C. (2010). Delta allometry: Growth laws for river deltas. *Geophysical Research Letters*, *37*(21). https://doi.org/10.1029/2010GL044592

Wright, L. D. (1985). River deltas. In R. A. Davis (Ed.), *Coastal sedimentary environments* (pp. 1–76). Springer New York. https://doi.org/10.1007/978-1-4612-5078-4_1

Zhou, Z., Chen, L., Tao, J., Gong, Z., Guo, L., Wegen, M., et al. (2020). The role of salinity in fluvio-deltaic morphodynamics: A long-term modelling study. *Earth Surface Processes and Landforms*, *45*(3), 590–604. https://doi.org/10.1002/esp.4757

References From the Supporting Information

Bagnold, R. A. (1966). An approach to the sediment transport problem from general physics. *Professional Paper*. https://doi.org/10.3133/pp422I

Bosboom, J., Reniers, A., & Luijendijk, A. (2014). On the perception of morphodynamic model skill. *Coastal Engineering*, *94*, 112–125. https://doi.org/10.1016/j.coastaleng.2014.08.008

Canestrelli, A., Nardin, W., Edmonds, D., Fagherazzi, S., & Slingerland, R. (2014). Importance of frictional effects and jet instability on the morphodynamics of river mouth bars and levees. *Journal of Geophysical Research: Oceans*, *119*(1), 509–522. https://doi.org/10.1002/2013JC009312

Google Earth 10.55.0.1. (2023a). Haliacmon river mouth 40°29'21"n 22°37'48"e. Retrieved from https://earth.google.com/web/

Google Earth 10.55.0.1. (2023b). Keum river mouth 36°00'12"n 126°38'22"e. Retrieved from https://earth.google.com/web/

Google Earth 10.55.0.1. (2023c). Manawatu river mouth 40°18'07"s 175°13'37"e. Retrieved from https://earth.google.com/web/

Google Earth 10.55.0.1. (2023d). Porong river mouth 7°31'37"s 112°51'00"e. Retrieved from https://earth.google.com/web/

Google Earth 10.55.0.1. (2023e). Rhône river mouth 43°20'46"n 4°49'52"e. Retrieved from https://earth.google.com/web/

Houston, J. R. (1995). Beach-fill volume required to produce specified dry beach width. *Coastal Engineering Technical Note*, 11–32. Retrieved from http://hdl.handle.net/11681/2135

Ikeda, S. (1982). Incipient motion of sand particles on side slopes. *Journal of Hydraulic Engineering*, *108*(1), 95–114. https://doi.org/10.1061/jyceaj.0005812

Kamphuis, J. W. (1991). Alongshore sediment transport rate. *Journal of Waterway, Port, Coastal, and Ocean Engineering*, *117*(6), 624–640. https://doi.org/10.1061/(ASCE)0733-950X(1991)117:6(624)

Kim, T., Choi, B., & Lee, S. (2006). Hydrodynamics and sedimentation induced by large-scale coastal developments in the Keum river estuary, Korea. Estuarine. *Coastal and Shelf Science*, *68*(3), 515–528. https://doi.org/10.1016/j.ecss.2006.03.003

Lesser, G. (2009). *An approach to medium-term coastal morphological modelling (Unpublished doctoral dissertation)*. TU Delft.

Mariotti, G., Falcini, F., Geleynse, N., Guala, M., Sun, T., & Fagherazzi, S. (2013). Sediment eddy diffusivity in meandering turbulent jets: Implications for levee formation at river mouths. *Journal of Geophysical Research: Earth Surface*, *118*(3), 1908–1920. https://doi.org/10.1002/jgrf.20134

Soulsby, R. (1997). *Dynamics of marine sands*. T. Telford London.

Uittenbogaard, R., & Vossen, B. (2004). Subgrid-scale model for quasi-2d turbulence in shallow water. *Shallow flows*, 575–582. https://doi.org/10.1201/9780203027325.ch72